Medical Image Analysis 57 (2019) 72–88

Contents lists available at ScienceDirect

Medical Image Analysis

journal homepage: www.elsevier.com/locate/media

Hierarchical spherical deformation for cortical surface registration

Ilwoo Lyu[a,*], Hakmook Kang[b], Neil D. Woodward[c], Martin A. Styner[d,e], Bennett A. Landman[a,c]

[a] Electrical Engineering and Computer Science, Vanderbilt University, Nashville, TN 37235, USA
[b] Department of Biostatistics, Vanderbilt University Medical Center, Nashville, TN 37203, USA
[c] Department of Psychiatry and Behavioral Sciences, Vanderbilt University Medical Center, Nashville, TN 37232, USA
[d] Department of Computer Science, The University of North Carolina at Chapel Hill, Chapel Hill, NC 27599, USA
[e] Department of Psychiatry, The University of North Carolina at Chapel Hill, Chapel Hill, NC 27514, USA

ARTICLE INFO

Article history:
Received 9 October 2018
Revised 30 April 2019
Accepted 24 June 2019
Available online 29 June 2019

Keywords:
Cortical surface registration
Shape correspondence
Spherical deformation
Spherical harmonics

ABSTRACT

We present hierarchical spherical deformation for a group-wise shape correspondence to address template selection bias and to minimize registration distortion. In this work, we aim at a continuous and smooth deformation field to guide accurate cortical surface registration. In conventional spherical registration methods, a global rigid alignment and local deformation are independently performed. Motivated by the composition of precession and intrinsic rotation, we simultaneously optimize global rigid rotation and non-rigid local deformation by utilizing spherical harmonics interpolation of local composite rotations in a single framework. To this end, we indirectly encode local displacements by such local composite rotations as functions of spherical locations. Furthermore, we introduce an additional regularization term to the spherical deformation, which maximizes its rigidity while reducing registration distortion. To improve surface registration performance, we employ the second order approximation of the energy function that enables fast convergence of the optimization. In the experiments, we validate our method on healthy normal subjects with manual cortical surface parcellation in registration accuracy and distortion. We show an improved shape correspondence with high accuracy in cortical surface parcellation and significantly low registration distortion in surface area and edge length. In addition to validation, we discuss parameter tuning, optimization, and implementation design with potential acceleration.

1. Introduction

Cortical morphometric approaches have been widely investigated in neuroimaging studies of brain development and atrophy such as gyrification (Armstrong et al., 1995; Schmitt et al., 2002; Luders et al., 2004; Harris et al., 2004; Gaser et al., 2006; Lui et al., 2011; Kim et al., 2016; Lyu et al., 2018b). In these studies, a well-established shape correspondence is a must to reveal global or local developmental trajectories over age or anatomical changes, and their relationships with cognitive functions or genetic and environmental factors. A shape correspondence is generally established by finding a proper mapping between cortical shapes via surface registration. However, the main challenge comes from inter-variability of cortical anatomies accompanied by a complicated, dynamic folding process that hampers establishing a shape correspondence appropriately. To find a cortical shape correspondence, surface registration generally involves registration metric, surface parametrization, and deformation estimation in the parametric space.

Surface registration is the process of transforming a cortical surface(s) to find an optimal alignment with a target cortical surface. Recent advance in 3D surface reconstruction (Dale et al., 1999; Cointepas et al., 2001; Kim et al., 2005; Huo et al., 2016) provides a better representation of cortical shapes than that of volumetric images, which enables the use of geometry on 2-manifolds for cortical surface registration. This can readily provide rich cortical geometric information such as curvature and even advanced cortical anatomical biomarkers. For example, curves along sulcal fundi have been used as robust features for a shape correspondence since they can reduce spatial ambiguity and increase morphological consistency (Thompson et al., 2004; Van Essen, 2005; Joshi et al., 2007; Shi et al., 2009; Lyu et al., 2010; 2018c). To establish a shape correspondence, several studies utilized anatomical biomarkers to evaluate spatial agreements of cortical surfaces (Tao et al., 2002; Thompson et al., 2004; Van Essen, 2005; Glaunès et al., 2004; Joshi et al., 2007; Park et al., 2012; Datar et al., 2013; Auzias et al., 2013; Lyu et al., 2015; Choi et al., 2015; Agrawal et al.,

* Corresponding author.
E-mail address: ilwoo.lyu@vanderbilt.edu (I. Lyu).

https://doi.org/10.1016/j.media.2019.06.013
1361-8415/

2017). Such a high level of distinctive shape description generally leads to less ambiguity in surface registration. In this framework, however, consistency in biomarker extraction directly influences the quality of a shape correspondence. Typically, sparse biomarkers are unable to fully cover the entire cortex for a dense correspondence. On the other hand, establishing dense biomarkers on a large population is practically implausible, and there almost always exists inter- and intra-variability of biomarker extraction even across well-trained experts.

Biomarker-free approaches (Fischl et al., 1999; Yeo et al., 2010; Lombaert et al., 2013; Robinson et al., 2018; Lyu et al., 2018a) have been emerging to overcome the inherent limitations in biomarker selection. These methods typically seek an optimal alignment of geometric feature maps that cover the entire cortex. Although these features potentially have more ambiguity than well-defined biomarkers in surface registration, their availability and clear definition can be a quite appealing candidate for registration metrics. To enhance feature description more distinctively, Lombaert et al. (2013), Wright et al. (2015), Orasanu et al. (2016), and Gahm et al. (2018) utilized spectral features defined in the Laplacian embedding or Tardif et al. (2015) and Robinson et al. (2018) used multi-modal features.

In addition to registration metric, another component in surface registration is a valid parametrization of cortical surfaces to handle surface registration tractably. There have been several attempts at parametrizing cortical shapes in a well-known space including planar (Hurdal et al., 2000; Joshi et al., 2007; Auzias et al., 2013), hyperbolic (Tsui et al., 2013; Shi et al., 2017) or spherical parametrization (Fischl et al., 1999; Tao et al., 2002; Glaunès et al., 2004; Robbins et al., 2004; Van Essen, 2005; Yeo et al., 2010; Choi et al., 2015; Robinson et al., 2018; Lyu et al., 2018a). These approaches provide easy handling of cortical surfaces via a consistent parametric representation, which simplifies the cortical shape correspondence problem. Of these attempts, spherical parametrization has been widely used for cortical surface registration since a reconstructed cortical surface typically has a genus-zero closed form. Thus, a sphere can naturally simplify a cortical surface while preserving its topology. Although mapping distortion always exists, its influence can be often minimized via conformal or area-preserving mappings (Fischl et al., 1999; Haker et al., 2000; Quicken et al., 2000; Tosun et al., 2004; Gu et al., 2004). Alternatively, a non-parametric shape correspondence using particle ensemble avoids a particular surface parametrization (Cates et al., 2007; Oguz et al., 2009; Datar et al., 2013; Agrawal et al., 2017). However, a full shape correspondence is implicit in that it only provides a particle correspondence. The resulting correspondence solely depends on the number of particles; no explicit deformation field is available.

In spherical mapping, a deformation field is obtained by finding displacements (or tracing velocity fields) on the sphere. Dale et al. (1999) and Robbins et al. (2004) optimized a cortical alignment to pursue explicit penalization of registration metric and distortion. Glaunès et al. (2004) proposed interpolation on a spherical vector field. Later Yeo et al. (2010) developed Spherical Demons with the interpolation technique proposed by Glaunès et al. (2004). In their method, spherical displacements are represented as local geodesics in the local tangent space. Each individual trajectory is obtained over a static velocity field to deform the sphere. Wheland and Pantazis (2014); Robinson et al. (2018) proposed pre-defined displacements around each sampling point on the sphere. The resulting deformation concatenates successive deformations to yield final deformation by optimizing over a discrete displacement field. Zou et al. (2007) and Park et al. (2012) applied a spherical thin-plate spline for a dense shape correspondence. Overall, these methods achieved successful cortical surface registration in a sense of well-aligned feature maps or anatomical biomarkers.

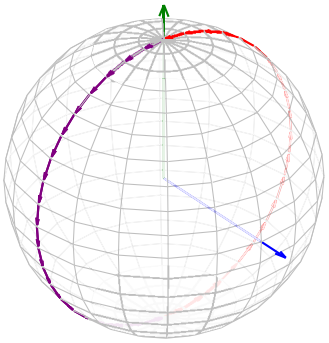

Fig. 1. An example of angular interpolation failures. The displacements by a counter clockwise rotation about the fixed axis (*blue*) are represented by elevation angles passing through the pole (*green*). Such angles have different signs before and after the pole (*red* and *purple*). The resulting interpolation thus yields rotation singularity at the pole, which is incapable of encoding the rotation completely. (For interpretation of the references to color in this figure legend, the reader is referred to the web version of this article.)

An important characteristic in spherical deformation is a rigid rotation of the 3D rotation group SO(3) that preserves relative distances and thus maximizes a feature alignment on the sphere without any distortion. Lack of a sufficient rigid rotation could end up with large registration distortion or locally optimal solution. High registration accuracy even with a perfect feature matching does not guarantee minimal registration distortion. Yet, there has been a gap between a global rigid alignment and local deformation in surface registration. In most spherical surface registration methods, a global rigid rotation is seldom incorporated during the optimization. A rigid alignment of feature maps is only performed independently before the optimization or based on volumetric transformation, and then only local displacements are optimized. One can interchangeably update a rigid alignment and local deformation during the optimization. However, the energy function needs to be carefully designed in this context; its optimization might be non-trivial (e.g., gradients of the energy function), otherwise. In our earlier work (Lyu et al., 2015), we proposed spherical harmonics interpolation of partial angular displacements in that spherical harmonics naturally encode global and local behaviors on the sphere. Unfortunately, the estimated deformation field depends on a particular spherical parametrization. This is true since linear interpolation of polar angles does not hold rigid rotations as shown in Fig. 1. Consequently, the method requires an optimal pole selection to reduce such rotation singularity around the poles. The solution was ad-hoc, which cannot fundamentally address such inconsistent interpolation.

In this paper, we propose novel spherical deformation that minimizes registration distortion. The proposed method couples rigid and non-rigid deformation in a single framework. In particular, the proposed method simultaneously achieves both a global rigid alignment and local deformation by allowing spatially varying rotations as functions of spherical locations. To avoid a bias toward template selection, we further propose a group-wise registration framework, in which a population statistics is estimated. The proposed method is inspired by our earlier approach to spherical harmonics interpolation of a deformation field (Lyu et al., 2015). Unlike this approach, the proposed method interpolates local composite rotations rather than polar angles that depend on a particular spherical coordinate system. This thus yields a well-established shape correspondence with low registration distortion. We extend our previous work (Lyu et al., 2018a) with the following main contributions: (1) detailed descriptions, (2) mathematical reformulation and derivation, (3) improved methodology (rigidity control

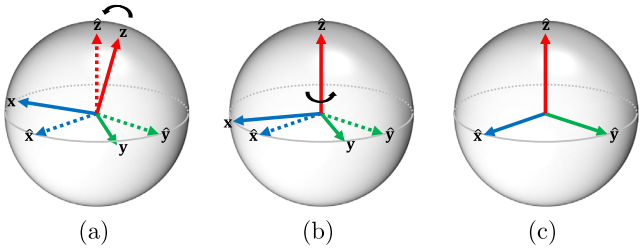

Fig. 2. Precession and intrinsic rotation: (a) initial setting of two frames, (b) **z**-axis alignment after precession, and (c) the final alignment after intrinsic rotation. Any rigid rotation can be implemented by precession and intrinsic rotation. The resulting composite rotation does not rely on a particular spherical coordinate system.

and optimization), and (4) extensive evaluation on a healthy subject dataset with manual cortical parcellation.

2. Methods

2.1. Problem definition

Consider a set of N cortical surfaces with their initial spherical mappings. For the nth subject, the goal is to estimate a continuous spherical deformation field $M^n : \mathbb{S}^2 \to \mathbb{S}^2$ such that

$$M^1(\mathbf{p}^1) = M^2(\mathbf{p}^2) = \cdots = M^N(\mathbf{p}^N)\,, \tag{1}$$

where $\mathbf{p}^n \in \mathbb{S}^2 = \{\mathbf{p} \in \mathbb{R}^3 : \|\mathbf{p}\| = 1\}$ is the corresponding location of the nth subject. M provides displacements carrying any spherical locations to their corresponding ones. Here, we pursue spherical displacements of the corresponding locations with reduced registration distortion. In the following sections, we first describe the proposed displacement encoding scheme represented by a rigid rotation and then extend the idea to non-rigid deformation.

2.2. Displacement encoding

We seek a consistent displacement encoding scheme independent of a non-linear spherical polar coordinate system. Here, such a displacement can be efficiently encoded by two successive rotations: rotation of an Euler axis (precession) followed by rotation about the Euler axis (intrinsic rotation).

Theorem 1. *For $\forall \mathbf{R} \in SO(3)$ with an arbitrary reference Euler axis* **z**, **R** *is sufficiently represented by the composition of two successive rotations: precession and intrinsic rotation.*

Proof. We consider initial and target (after **R**) frames denoted by **F** and $\hat{\mathbf{F}}$, respectively; i.e., $\hat{\mathbf{F}} = \mathbf{R} \cdot \mathbf{F}$. Without loss of generality, let $\mathbf{F} = [\mathbf{x}\ \mathbf{y}\ \mathbf{z}]$ and $\hat{\mathbf{F}} = [\hat{\mathbf{x}}\ \hat{\mathbf{y}}\ \hat{\mathbf{z}}]$. (1) Precession: we rotate **z** to coincide with $\hat{\mathbf{z}}$. After this, other two axes are on the $\hat{\mathbf{x}}\hat{\mathbf{y}}$ plane, which reduces one degree of freedom. (2) Intrinsic rotation: since **z** is aligned to $\hat{\mathbf{z}}$, there exists a proper rotation angle about $\hat{\mathbf{z}}$ to fit **F** to $\hat{\mathbf{F}}$. Therefore, the two rotations are sufficient to encode **R**. See Fig. 2 for such a composite rotation. □

Theorem 1 states that two successive rotations (of and about an Euler axis) can vary depending on a reference Euler axis but their composite rotation is equivalent to any target rotation independent of a reference Euler axis. Any reference Euler axis can sufficiently render a target rigid rotation. This further implies that any spherical displacement can be obtained by finding two successive rotations regardless of a reference Euler axis. Therefore, we do not assume a specific reference Euler axis in this work. Fig. 3 shows a schematic illustration of the proposed encoding. For notational simplicity, we model these rotations by the axis-angle representation (matrix exponential) throughout this paper.

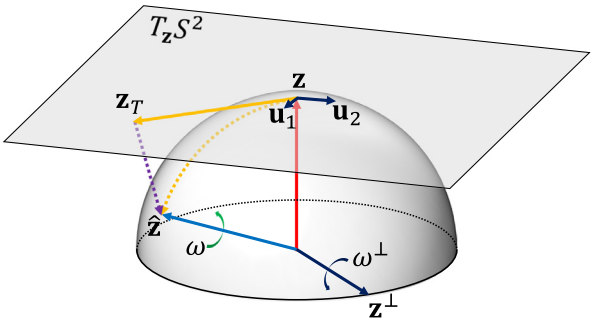

Fig. 3. A schematic illustration of the proposed rotation by the axis-angle representation. For the rotation of a given location, (precession) the rotation axis **z** (*red*) is rotated to $\hat{\mathbf{z}}$ (*blue*) by $\omega^\perp$ about $\mathbf{z}^\perp$, followed by (intrinsic rotation) a rotation about $\hat{\mathbf{z}}$ by ω (*green*). The exponential map (*purple*) at **z** is employed to encode local geodesics (*orange*). Finally, the rotation axis $\hat{\mathbf{z}}$ and its associated rotation angle ω smoothly vary on the unit sphere as functions of spherical locations. A half sphere is used for better visualization. (For interpretation of the references to color in this figure legend, the reader is referred to the web version of this article.)

2.2.1. Precession: Rotation of Euler axis

Consider a reference Euler axis $\mathbf{z} \in \mathbb{S}^2$ is rotated to be at a target axis $\hat{\mathbf{z}} \in \mathbb{S}^2$. Intuitively, this is equivalent to precession of **z** determined by axis tilt of **z**. For spherical polar coordinates $(\theta, \phi) \in [0, \pi] \times [-\pi, \pi]$, we define their transformation into Cartesian coordinates.

$$\varphi(\theta, \phi) = [\sin\theta\cos\phi, \sin\theta\sin\phi, \cos\theta]^T. \tag{2}$$

In a naive way, the location of $\hat{\mathbf{z}}$ is represented as a function of angular displacements $(\Delta\theta, \Delta\phi)$.

$$\hat{\mathbf{z}} = \varphi(\theta_{\mathbf{z}} + \Delta\theta, \phi_{\mathbf{z}} + \Delta\phi), \tag{3}$$

where $\theta_{\mathbf{z}}$ and $\phi_{\mathbf{z}}$ are inclination and azimuth of **z**, respectively. Unfortunately, $\Delta\theta$ and $\Delta\phi$ are dependent and vary with respect to the location of **z** for the same distance of geodesics. To consistently handle displacements without angular dependency, we instead compute $\hat{\mathbf{z}}$ as a function of geodesics on the local tangent plane at **z** via an exponential map $\exp_{\mathbf{z}} : T_{\mathbf{z}}\mathbb{S}^2 \to \mathbb{S}^2$. In this way, we can thus find a unique location $\mathbf{z}_T \in T_{\mathbf{z}}\mathbb{S}^2$ that corresponds to $\hat{\mathbf{z}}$. For two arbitrary orthonormal bases $\mathbf{u}_1, \mathbf{u}_2 \in T_{\mathbf{z}}\mathbb{S}^2$, $\hat{\mathbf{z}}$ is obtained by a linear combination of the two bases:

$$\hat{\mathbf{z}} = \exp_{\mathbf{z}}(\mathbf{z}_T) = \exp_{\mathbf{z}}(c_{\mathbf{u}_1}\mathbf{u}_1 + c_{\mathbf{u}_2}\mathbf{u}_2), \tag{4}$$

where $c_{\mathbf{u}_1}$ and $c_{\mathbf{u}_2}$ are coefficients associated with $\mathbf{u}_1$ and $\mathbf{u}_2$, respectively. Note that $\mathbf{u}_1$ and $\mathbf{u}_2$ define a reference frame on the tangent space, which has no influence on geodesics themselves on $T_{\mathbf{z}}\mathbb{S}^2$. To rotate **z** to $\hat{\mathbf{z}}$, we define an additional rotation axis $\mathbf{z}^\perp$ and its rotation angle $\omega^\perp$ as follows:

$$\mathbf{z}^\perp = \frac{\mathbf{z} \times \hat{\mathbf{z}}}{\|\mathbf{z} \times \hat{\mathbf{z}}\|} \text{ and } \omega^\perp = \arccos(\mathbf{z}^T \cdot \hat{\mathbf{z}}). \tag{5}$$

Since the exponential map is defined on the sphere and $\mathbf{z} \perp \mathbf{z}_T$, this further simplifies Eq. (5):

$$\mathbf{z}^\perp = \frac{\mathbf{z} \times \mathbf{z}_T}{\sqrt{c_{\mathbf{u}_1}^2 + c_{\mathbf{u}_2}^2}} \text{ and } \omega^\perp = \sqrt{c_{\mathbf{u}_1}^2 + c_{\mathbf{u}_2}^2}. \tag{6}$$

Let $[\,\cdot\,]_\times$ denote a 3-by-3 skew-symmetric matrix to represent a cross product. We have the rotation of **z** as a matrix exponential

$$\mathbf{R}_1 = \exp(\omega^\perp [\mathbf{z}^\perp]_\times) = \exp([\mathbf{z} \times \mathbf{z}_T]_\times). \tag{7}$$

2.2.2. Intrinsic rotation: Rotation about Euler axis

Given a rotation angle $\omega \in [-\pi, \pi]$ about $\hat{\mathbf{z}}$, we have the intrinsic rotation of $\hat{\mathbf{z}}$ as a matrix exponential

$$\mathbf{R}_2 = \exp(\omega [\hat{\mathbf{z}}]_\times). \tag{8}$$

From Eqs. (7) and (8), the overall composite rotation is given by

$$\mathbf{R}(c_{\mathbf{u}_1}, c_{\mathbf{u}_2}, \omega) = \mathbf{R}_2 \cdot \mathbf{R}_1 = \exp(\omega[\hat{\mathbf{z}}]_\times) \cdot \exp([\mathbf{z} \times \mathbf{z}_T]_\times). \tag{9}$$

For $\forall \mathbf{p} \in \mathbb{S}^2$, this encodes a new location:

$$M(\mathbf{p}) = \hat{\mathbf{p}}(c_{\mathbf{u}_1}, c_{\mathbf{u}_2}, \omega) = \mathbf{R}(c_{\mathbf{u}_1}, c_{\mathbf{u}_2}, \omega) \cdot \mathbf{p}. \tag{10}$$

The resulting deformation M yields an identical rigid rotation at every location and globally drives the corresponding locations to the closest location by finding an optimal set of $c_{\mathbf{u}_1}$, $c_{\mathbf{u}_2}$, and ω.

2.3. Extension to hierarchical spherical deformation

In general, all the corresponding locations are not completely aligned after the rigid rotation. This leads to an extension of the rigid rotation to non-rigid deformation. From the observation of spatial homogeneity in feature maps, we here propose spatially varying rotations as functions of spherical locations rather than constants. The idea is to smoothly interpolate composite rotations over the sphere. For this purpose, we use a spherical harmonics interpolation technique that allows smooth interpolation of signals defined on the unit sphere. At a spherical location $\varphi(\theta, \phi)$, the spherical harmonics basis function of degree l and order m ($-l \le m \le l$) is given by

$$Y_l^m(\theta, \phi) = \sqrt{\frac{2l+1}{4\pi} \frac{(l-m)!}{(l+m)!}} P_l^m(\cos\theta) e^{im\phi}, \tag{11}$$

$$Y_l^{-m}(\theta, \phi) = (-1)^m Y_l^{m*}(\theta, \phi), \tag{12}$$

where Y_l^{m*} denotes the complex conjugate of Y_l^m, and P_l^m is the associated Legendre polynomial

$$P_l^m(x) = \frac{(-1)^m}{2^l l!} (1-x^2)^{\frac{m}{2}} \frac{d^{(l+m)}}{dx^{(l+m)}} (x^2-1)^l. \tag{13}$$

A real form of the functions is sufficient in this framework.

$$Y_{l,m} = \begin{cases} \frac{1}{\sqrt{2}}(Y_l^m + (-1)^m Y_l^{-m}) & m > 0, \\ Y_l^0 & m = 0, \\ \frac{1}{\sqrt{2}i}(Y_l^{-m} - (-1)^m Y_l^m) & m < 0. \end{cases} \tag{14}$$

In particular, $\hat{\mathbf{z}}$ is obtained by plugging a set of spherical harmonics coefficients $\mathbf{c}_{\mathbf{u}_1} = \{c_{l,\mathbf{u}_1}^m\}$ and $\mathbf{c}_{\mathbf{u}_2} = \{c_{l,\mathbf{u}_2}^m\}$ into Eq. (4):

$$\hat{\mathbf{z}}(\theta, \phi) = \exp_{\mathbf{z}} \left(\sum_{l=0}^{\infty} \sum_{m=-l}^{l} \left(c_{l,\mathbf{u}_1}^m \mathbf{u}_1 + c_{l,\mathbf{u}_2}^m \mathbf{u}_2 \right) \cdot Y_{l,m}(\theta, \phi) \right). \tag{15}$$

This also redefines $\mathbf{z}_T$ as a function of a spherical location $\varphi(\theta, \phi)$. In addition, ω is linearly proportional to the amount of intrinsic rotation. Thus, ω can be also obtained by the spherical harmonics interpolation as a function of spherical harmonics coefficients $\mathbf{c}_\omega = \{c_{l,\omega}^m\}$.

$$\omega(\theta, \phi) = \sum_{l=0}^{\infty} \sum_{m=-l}^{l} c_{l,\omega}^m \cdot Y_{l,m}(\theta, \phi). \tag{16}$$

This locally defines a rotation about $\hat{\mathbf{z}}$ at each spherical location $\varphi(\theta, \phi)$, which implies that the rotation smoothly changes across spherical locations. The proposed deformation is hierarchically represented since the spherical harmonics basis functions are linearly independent; the lower spherical harmonics degree, the smoother, more global deformation. Thus, the smoothness is easily controllable. Note that the deformation is equivalent to a rigid (global) rotation if $l = 0$.

2.4. Optimization

2.4.1. Energy function

We use scalar maps (e.g., mean curvature) defined on the cortical surfaces for the registration metric. We evaluate the agreement of the deformed scalar maps on the unit sphere to find the optimal local composite rotations. Since an explicit correspondence of scalar maps is unavailable, we instead put S icosahedral sampling points on each subject's sphere and evaluate the agreement of the deformed scalar maps at the corresponding sampling locations. Given estimates of $\mathbf{c}_{\mathbf{u}_1}^n, \mathbf{c}_{\mathbf{u}_2}^n, \mathbf{c}_\omega^n$ of the nth subject, we consider its deformed scalar map f^n and the corresponding location $\mathbf{p}_i^n$ to the ith sampling location $\mathbf{p}_i$ such that $\mathbf{p}_i = \mathbf{R}(\mathbf{c}_{\mathbf{u}_1}^n, \mathbf{c}_{\mathbf{u}_2}^n, \mathbf{c}_\omega^n) \cdot \mathbf{p}_i^n$ (see Eq. (10)). By letting $\bar{f}$ be the mean across scalar maps, the feature mismatching energy is given by

$$E_f(\mathbf{c}_{\mathbf{u}_1}, \mathbf{c}_{\mathbf{u}_2}, \mathbf{c}_\omega) = \frac{1}{2NS} \sum_{n=1}^{N} \sum_{i=1}^{S} \frac{\left(f^n(\hat{\mathbf{p}}_i^n) - \bar{f}_i\right)^2}{\sigma_{f,\hat{\mathbf{p}}_i^n}^2}, \tag{17}$$

where σ_f^2 is feature variance. This energy encodes the amount of mismatching across feature maps to the mean as the sum of the standard scores; for the perfect feature matching, the energy becomes zero. Yet, the rigidity in E_f is implicit. To encourage the rigidity of the deformation more explicitly, we consider additional distortion energy:

$$E_d(\mathbf{c}_{\mathbf{u}_1}, \mathbf{c}_{\mathbf{u}_2}, \mathbf{c}_\omega) = \frac{1}{2N} \sum_{n=1}^{N} \frac{1}{S_n} \sum_{i=1}^{S_n} \frac{\arccos^2\left(\hat{\mathbf{p}}_i^{nT} \cdot \tilde{\mathbf{p}}_i^n\right)}{\sigma_{d,\hat{\mathbf{p}}_i^n}^2}, \tag{18}$$

where S_n is the number of vertices of the nth subject, σ_d^2 is distortion prior, and $\tilde{\mathbf{p}}$ is the reconstructed location of $\hat{\mathbf{p}}$ at $l = 0$. This energy encodes the sum of the squared geodesic distance (arc length) distortion at $\hat{\mathbf{p}}$ between before and after non-rigid deformation; the energy is equal to zero if only rigid rotation is applied (i.e., $l = 0$). Thus, this term helps prevent the deformation from being hugely distorted and only optimized toward feature matching during the optimization. Given updated coefficients, this quantifies the amount of distortion from initial relative displacements. Overall, we have the following total energy function:

$$E(\mathbf{c}_{\mathbf{u}_1}, \mathbf{c}_{\mathbf{u}_2}, \mathbf{c}_\omega) = E_f(\mathbf{c}_{\mathbf{u}_1}, \mathbf{c}_{\mathbf{u}_2}, \mathbf{c}_\omega) + \alpha E_d(\mathbf{c}_{\mathbf{u}_1}, \mathbf{c}_{\mathbf{u}_2}, \mathbf{c}_\omega), \tag{19}$$

where $\alpha \in \mathbb{R}^+$ is a weighting factor. The total energy function leverages between a feature alignment and rigidity of the deformation. In the experiments, we balanced these energy terms ($\alpha = 1$).

2.4.2. Second order approximation

In this work, the energy function is minimized by a standard Levenberg-Marquardt optimizer (Levenberg, 1944; Marquardt, 1963). For this purpose, we use the second order approximation of the optimization for fast convergence on such least squares. Since the coefficients are independent between subjects, we compute Jacobian matrices $\mathbf{J}_f$ and $\mathbf{J}_d$ of each individual subject. For the nth subject, we have the following partial derivatives at $\hat{\mathbf{p}}_i = \varphi(\theta_{\hat{\mathbf{p}}_i}, \phi_{\hat{\mathbf{p}}_i})$ (see Appendix A for their derivation). For simplicity, we omit a superscript n here.

$$\begin{aligned} \frac{\partial \hat{\mathbf{p}}_i^T}{\partial c_{\mathbf{u}_1,j}} &= Y_j(\theta_{\hat{\mathbf{p}}_i}, \phi_{\hat{\mathbf{p}}_i}) \cdot \left([\mathbf{z} \times \mathbf{u}_1]_\times \cdot \hat{\mathbf{p}}_i\right)^T, \\ \frac{\partial \hat{\mathbf{p}}_i^T}{\partial c_{\mathbf{u}_2,j}} &= Y_j(\theta_{\hat{\mathbf{p}}_i}, \phi_{\hat{\mathbf{p}}_i}) \cdot \left([\mathbf{z} \times \mathbf{u}_2]_\times \cdot \hat{\mathbf{p}}_i\right)^T, \\ \frac{\partial \hat{\mathbf{p}}_i^T}{\partial c_{\omega,j}} &= Y_j(\theta_{\hat{\mathbf{p}}_i}, \phi_{\hat{\mathbf{p}}_i}) \cdot \left([\hat{\mathbf{z}}]_\times \cdot \hat{\mathbf{p}}_i\right)^T, \end{aligned} \tag{20}$$

where Y_j $(1 \le j \le (l+1)^2)$ is the jth spherical harmonics basis function. By assuming that $\bar{f}$ and σ_f^2 are constant, the ijth entry

of $\mathbf{J}_f$ is given by

$$J_{f,1} = \frac{\partial \hat{\mathbf{p}}_i^T}{\partial c_{\mathbf{u}_1,j}} \cdot \nabla_{\hat{\mathbf{p}}_i} f \cdot \frac{1}{\sigma_{f,\hat{\mathbf{p}}_i}},$$
$$J_{f,2} = \frac{\partial \hat{\mathbf{p}}_i^T}{\partial c_{\mathbf{u}_2,j}} \cdot \nabla_{\hat{\mathbf{p}}_i} f \cdot \frac{1}{\sigma_{f,\hat{\mathbf{p}}_i}}, \tag{21}$$
$$J_{f,3} = \frac{\partial \hat{\mathbf{p}}_i^T}{\partial c_{\omega,j}} \cdot \nabla_{\hat{\mathbf{p}}_i} f \cdot \frac{1}{\sigma_{f,\hat{\mathbf{p}}_i}}.$$

We have an S-by-$3(l+1)^2$ matrix $\mathbf{J}_f$.

$$\mathbf{J}_f = \left[\mathbf{J}_{f,1}, \mathbf{J}_{f,2}, \mathbf{J}_{f,3}\right], \tag{22}$$

and its residual $\mathbf{R}_f$ is given by

$$\mathbf{R}_f = \left[\frac{f(\hat{\mathbf{p}}_1) - \bar{f}_1}{\sigma_{f,\hat{\mathbf{p}}_1}}, \cdots, \frac{f(\hat{\mathbf{p}}_S) - \bar{f}_S}{\sigma_{f,\hat{\mathbf{p}}_S}}\right]^T. \tag{23}$$

Similarly, by assuming that $\tilde{\mathbf{p}}$ and σ_d^2 are constant, the ijth entry of $\mathbf{J}_d$ is represented by

$$J_{d,1} = \frac{\partial \hat{\mathbf{p}}_i^T}{\partial c_{\mathbf{u}_1,j}} \cdot \tilde{\mathbf{p}}_i \cdot \frac{-1}{\sqrt{1 - \left(\hat{\mathbf{p}}_i^T \cdot \tilde{\mathbf{p}}_i\right)^2}} \cdot \frac{1}{\sigma_{d,\hat{\mathbf{p}}_i}},$$
$$J_{d,2} = \frac{\partial \hat{\mathbf{p}}_i^T}{\partial c_{\mathbf{u}_2,j}} \cdot \tilde{\mathbf{p}}_i \cdot \frac{-1}{\sqrt{1 - \left(\hat{\mathbf{p}}_i^T \cdot \tilde{\mathbf{p}}_i\right)^2}} \cdot \frac{1}{\sigma_{d,\hat{\mathbf{p}}_i}}, \tag{24}$$
$$J_{d,3} = \frac{\partial \hat{\mathbf{p}}_i^T}{\partial c_{\omega,j}} \cdot \tilde{\mathbf{p}}_i \cdot \frac{-1}{\sqrt{1 - \left(\hat{\mathbf{p}}_i^T \cdot \tilde{\mathbf{p}}_i\right)^2}} \cdot \frac{1}{\sigma_{d,\hat{\mathbf{p}}_i}}.$$

An S_i-by-$3(l+1)^2$ matrix $\mathbf{J}_d$ has the following form.

$$\mathbf{J}_d = \left[\mathbf{J}_{d,1}, \mathbf{J}_{d,2}, \mathbf{J}_{d,3}\right], \tag{25}$$

and its residual $\mathbf{R}_d$ is given by

$$\mathbf{R}_d = \left[\frac{\arccos\left(\hat{\mathbf{p}}_1^T \cdot \tilde{\mathbf{p}}_1\right)}{\sigma_{d,\hat{\mathbf{p}}_1}}, \cdots, \frac{\arccos\left(\hat{\mathbf{p}}_{S_n}^T \cdot \tilde{\mathbf{p}}_{S_n}\right)}{\sigma_{d,\hat{\mathbf{p}}_{S_n}}}\right]^T. \tag{26}$$

Let $\mathtt{diag}(\cdot)$ denote a diagonal matrix. In a Levenberg-Marquardt framework, we have the following update step at each iteration of the optimization.

$$\Delta = -(\mathbf{H} + \lambda \mathtt{diag}(\mathbf{H}))^{-1}\left(\frac{1}{S}\mathbf{J}_f^T\mathbf{R}_f + \alpha\frac{1}{S_n}\mathbf{J}_d^T\mathbf{R}_d\right), \tag{27}$$

where λ is a damping factor, and

$$\mathbf{H} = \frac{1}{S}\mathbf{J}_f^T\mathbf{J}_f + \alpha\frac{1}{S_n}\mathbf{J}_d^T\mathbf{J}_d. \tag{28}$$

In practice, $3(l+1)^2 \ll S\,(S_n)$, which avoids rank deficiency. Finally, the spherical harmonics coefficients are updated at each iteration:

$$\mathbf{c} = \mathbf{c} + \delta\Delta, \tag{29}$$

where $\delta \in \mathbb{R}^+$ is regularization of the update step Δ to ensure that spheres are orientable (i.e., triangles with non-negative area in the implementation).

2.4.3. Optimization and criteria

Given a feature map, we update coefficients by increasing spherical harmonics degree from $l = 0$ for an initial guess (Lyu et al., 2015). At the beginning, the optimization is independently performed on each individual degree, which yields a roughly reasonable guess as a good starting point for the optimization. At the same time, we also estimate $\bar{f}$ and σ_f^2 from initial scalar maps and then update them after the initial guess to employ improved population statistics. Since σ_d^2 is hard to be estimated, we use a single constant for the entire cortex. Once coefficients and population statistics are obtained from the initial guess, all spherical harmonics coefficients are finally optimized together, which drives all the deformation fields by optimizing both rigid and non-rigid deformation. The optimization converges if the energy difference between two successive steps is less than 10^{-5}. We set $\lambda = 0.001$ and $\delta = 1$. Note that δ is a local variable for each individual subject to maintain its orientability. Algorithm 1 summarizes the proposed surface registration in each resolution[1].

Algorithm 1 Hierarchical Spherical Deformation.

Input: Spheres with $\mathbf{c}$, f, $\bar{f}$, σ_f^2, σ_d^2, and λ.
Output: Deformation fields M

for all l **do** ▷ Incremental optimization
  $\lambda \leftarrow 0.001$ ▷ Initialize the damping factor.
  repeat ▷ Minimize the energy of Eq. (19).
    for all spheres **do**
      $\delta \leftarrow 1$ ▷ Initialize the update scale.
      Compute spherical gradients of Eq. (20).
      Compute Jacobian matrices and residuals of Eqs. (22), (23), (25), and (26).
      Compute update step Δ of Eq. (27).
      repeat ▷ Ensure diffeomorphism
        Update coefficients $\mathbf{c}$ using Eq. (29).
        Update local composite rotations $\mathbf{R}$ using Eqs. (15) and (16).
        Update deformation field M using Eq. (10).
        if negative triangle area found **then**
          $\delta \leftarrow \delta/2$ ▷ Reduce the update scale.
        end if
      until ensure orientable spheres
    end for
    if E decreases **then** ▷ Eq. (19)
      $\lambda \leftarrow \lambda/2$ ▷ Reduce the damping factor.
    else
      $\lambda \leftarrow \lambda \cdot 2$ ▷ Increase the damping factor.
    end if
  until convergence
end for

2.4.4. Multi-resolution approach

It is widely acceptable in cortical surface registration frameworks (Fischl et al., 1999; Tao et al., 2002; Lyttelton et al., 2007; Zou et al., 2007; Yeo et al., 2010; Wheland and Pantazis, 2014; Lyu et al., 2018a) to utilize mean curvature of the cortical surfaces as a registration metric since it is mathematically well-defined and reasonably captures the overall cortical folding patterns. However, due to the high locality of mean curvature and the nonlinearity of the energy function, there could exist local optima during the optimization. To alleviate such a pitfall, we adapt a multi-resolution approach of different feature maps (Yeo et al., 2010). We use four geometric features from the cortex with different numbers of icosahedral sampling points on the sphere: mean curvature of the inflated surfaces (*lCurv*, $S = 2,562$), sparse sulcal depth of the cortical surfaces (*lSulc*, $S = 10,242$), dense sulcal depth of the cortical surfaces (*hSulc*, $S = 40,962$), and mean curvature of the cortical surfaces (*hCurv*, $S = 163,842$). Here, sparse and dense sulcal depth shares exactly the same geometric property but mapped onto the sphere with different levels of icosahedral subdivision of S. In this approach, we minimize the energy function of Eq. (19) for each resolution (feature) from *lCurv* to *hCurv*, where a deformation field is incrementally optimized starting from its estimation at the previous resolution. The proposed algorithm works well even in a single resolution as shown in Fig. 4 and Lyu et al. (2018a), but

[1] The code is available at https://github.com/ilwoolyu/HSD.

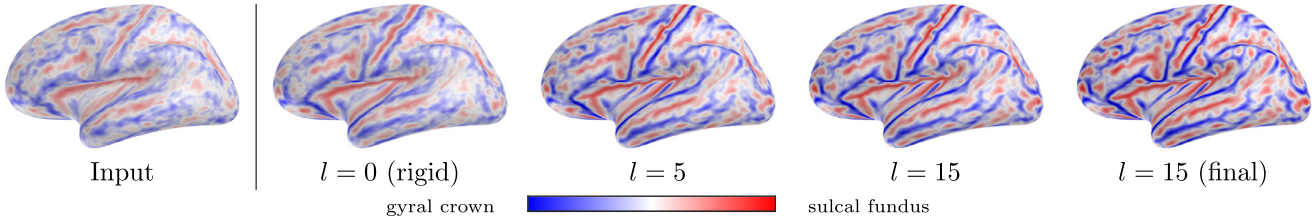

Fig. 4. The average *hCurv* feature maps at intermediate spherical harmonics degrees l (optimization with single resolution based on only *hCurv*). Each hemisphere shows the average *hCurv* feature after independent optimization at each individual degree. The cortical folding patterns become sharper, and the finest patterns are achieved after spherical harmonics coefficients are optimized together.

the multi-resolution approach generally gives better performance since the approach can offer a complementary feature alignment at each resolution from global to local perspectives. Once again, we call Algorithm 1 for each resolution by providing the previous estimated deformation fields (i.e., spherical harmonics coefficients). In the experiments, we initialized all the coefficients $\mathbf{c}$ to zero once at the lowest resolution (*lCurv*).

3. Results

3.1. Experimental setup

The evaluation of cortical surface registration is quite challenging since no ground-truth shape correspondence is available on the human cortices in general. Although the overlap of cortical parcellation may not be a gold standard to fully evaluate the performance of cortical surface registration (Mangin et al., 2016), it can yield broad interests in ROI-based clinical, functional and structural studies. Thus, we focused on the overlap of cortical parcellation as one of the metrics of surface registration performance in this work.

There exists a well-known public dataset with manual labels of 31 cortical regions (based on the DKT-31 protocol) on 101 healthy subjects called Mindboggle-101 (Klein and Tourville, 2012)[2]. The dataset was well validated, and its size is relatively large for the evaluation. However, the cortical surface parcellation on this dataset was created via the shape correspondence established by FreeSurfer (Fischl et al., 1999) and then manually corrected by experts. This could have a potential bias toward that specific method. Another full dataset is publicly available from the MICCAI 2012 Grand Challenge and Workshop on Multi-Atlas Labeling (Landman and Warfield, 2012)[3]. The dataset consists of 30 healthy subjects with 35 scans out of the OASIS dataset (Marcus et al., 2007). As ground-truth used in the MICCAI 2012 Grand Challenge and Workshop on Multi-Atlas Labeling, these images have been intensively delineated and corrected by neuroanatomists with 133 labels (132 regions including subcortical structures and 1 background) via the BrainCOLOR protocol (Klein et al., 2010)[4]. Thus, the cortical labels are completely independent of any of surface registration methods. However, the labels were only delineated on the volumetric images that require additional projection onto the cortical surfaces.

Although both datasets have their own issues, in this work, we evaluated our method mainly on the latter dataset with BrainCOLOR to ensure independent cortical surface parcellation for fair comparisons. On the other hand, Mindboggle-101 was used only to provide reference validation of cortical parcellation, and the experimental results on this dataset are available as supplementary information. Since the latter dataset with BrainCOLOR includes two repeat scans for 5 subjects, we excluded the repeat scans for these subjects to prevent potential bias toward them. Therefore, 30 scans were used with their manual labels in total. Finally, an expert manually corrected the cortical parcellation across the 30 scans since the label projection from volume to surface has a potential misalignment due to quantization errors. After the projection, a total of 49 cortical ROIs (only gray matter tissue labels) are available as shown in Table 1.

The cortical surfaces were reconstructed via a standard FreeSurfer pipeline (Dale et al., 1999), and both left and right hemispheres were used for evaluation. Since our method adapted the multi-resolution registration (including feature maps) of FreeSurfer (Fischl et al., 1999) and Spherical Demons (Yeo et al., 2010), we compared our method with the two methods. We used their suggested (and widely adapted) parameter settings on healthy populations. All experiments were conducted with a single thread (Intel Xeon E5-2630 2.20GHz). The evaluation was based on a feature alignment, cortical parcellation, and registration distortion. In particular, we first evaluated the three methods in a pair-wise manner to evaluate spherical deformation itself and then evaluated them in a group-wise manner to ensure minimal distortions, by which population average is iteratively updated (Lyttelton et al., 2007; Yeo et al., 2010). Once again, the cortical parcellation is completely independent of the three methods and was used only for evaluation since we did not include any information from the cortical parcellation during the optimization. In all of these methods, surface registration is ultimately achieved by maximizing the alignment of *hCurv* at the end of the optimization.

3.2. Pair-wise spherical deformation

We first focused on a single resolution given a target template to evaluate pure spherical deformation performance for each method in a pair-wise manner since a multi-resolution approach has dependency between successive resolutions, which is challenging to evaluate the spherical deformation itself. Specifically, we evaluated the three methods for their flexibility (ability to overcome local optima) of deformation with only an *hCurv* feature that has locally homogeneous regions. Surface registration with a single feature may be neither quite common practice nor necessarily optimal in neuroanatomy. However, it would be useful (1) to observe spherical deformation even on highly localized features that most likely suffer from local optima and (2) to evaluate a balance between registration accuracy and distortion. In this context, we evaluated the three methods in feature alignment and registration distortion. Note that we used exactly the same feature maps and FreeSurfer's standard template (so-called fsaverage (Fischl et al., 1999)) for the three methods, and all these methods perform their own optimal rigid alignment before the non-rigid deformation. In our method, we set a high level of icosahedral subdivision $S = 163,842$ and $l = 15$. To see an advantage of the proposed harmonized rigid alignment, we performed our method

[2] The dataset is available at https://mindboggle.info/.

[3] Request for the data acquisition with manual labels at https://my.vanderbilt.edu/masi/workshops/.

[4] See more information about the BrainCOLOR protocol at Neuromorphometrics, Inc. http://www.neuromorphometrics.com/.

Table 1
49 cortical regions of the BrainCOLOR protocol.

Acronym	Region	Acronym	Region	Acronym	Region
ACgG	Anterior cingulate gyrus	AIns	Anterior insula	AOrG	Anterior orbital gyrus
AnG	Angular gyrus	Calc	Calcarine cortex	CO	Central operculum
Cun	Cuneus	Ent	Entorhinal area	FO	Frontal operculum
FRP	Frontal pole	FuG	Fusiform gyrus	GRe	Gyrus rectus
IOG	Inferior occipital gyrus	ITG	Inferior temporal gyrus	LiG	Lingual gyrus
LOrG	Lateral orbital gyrus	MCgG	Middle cingulate gyrus	MFC	Medial frontal cortex
MFG	Middle frontal gyrus	MOG	Middle occipital gyrus	MOrG	Medial orbital gyrus
MPoG	Postcentral gyrus medial segment	MPrG	Precentral gyrus medial segment	MSFG	Superior frontal gyrus medial segment
MTG	Middle temporal gyrus	OCP	Occipital pole	OFuG	Occipital fusiform gyrus
OpIFG	Opercular part of the inferior frontal gyrus	OrIFG	Orbital part of the inferior frontal gyrus	PCgG	Posterior cingulate gyrus
PCu	Precuneus	PHG	Parahippocampal gyrus	PIns	Posterior insula
PO	Parietal operculum	PoG	Postcentral gyrus	POrG	Posterior orbital gyrus
PP	Planum polare	PrG	Precentral gyrus	PT	Planum temporale
SCA	Subcallosal area	SFG	Superior frontal gyrus	SMC	Supplementary motor cortex
SMG	Supramarginal gyrus	SOG	Superior occipital gyrus	SPL	Superior parietal lobule
STG	Superior temporal gyrus	TMP	Temporal pole	TrIFG	Triangular part of the inferior frontal gyrus
TTG	Transverse temporal gyrus				

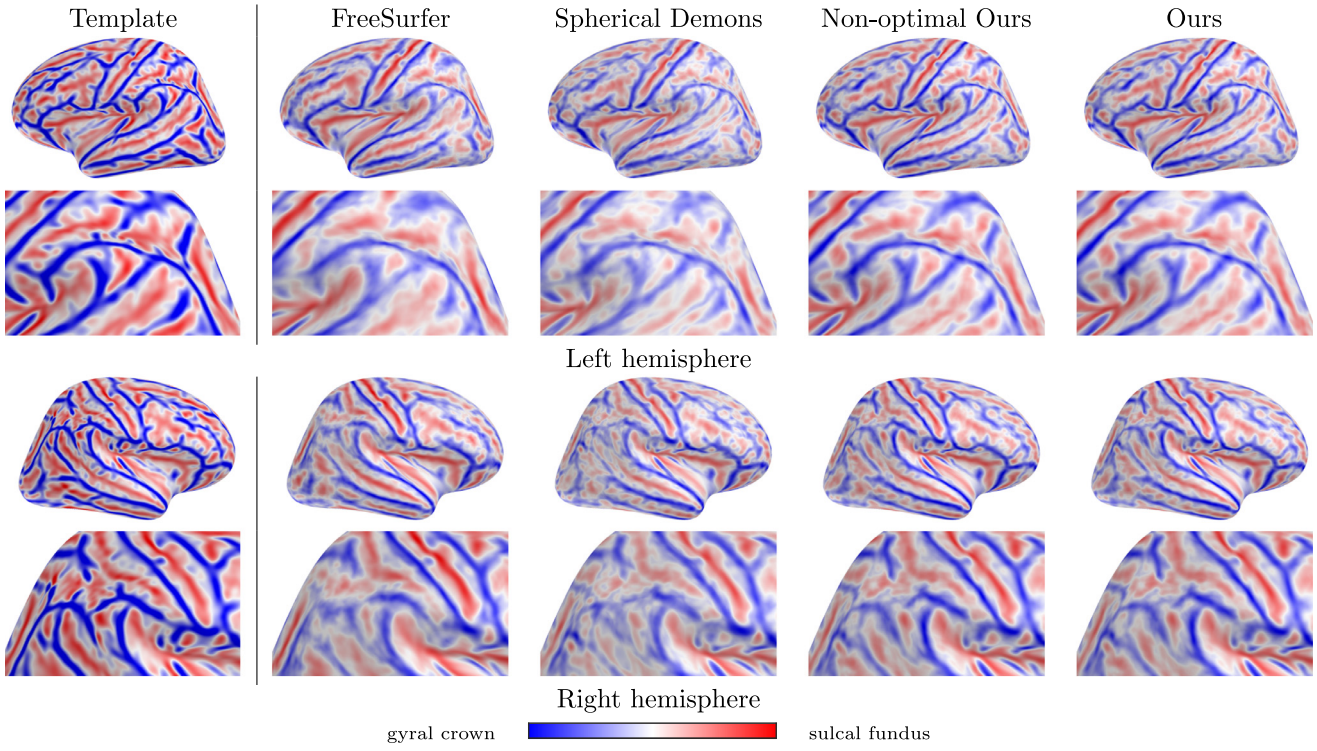

Fig. 5. The average *hCurv* feature maps on the 30 subjects after pair-wise registration to a fixed template. Overall, these methods achieve similar *hCurv* patterns. The proposed method including a non-optimal rigid alignment provides a sharper representation close to the template.

Table 2
hCurv variance. The proposed method achieves the smallest variance. Here we computed the variance at $l = 15$ for both hemispheres. It is noteworthy that this statistics only evaluates spherical deformation itself; i.e., the energy of feature mismatching in these methods between subjects and a given template.

Hemisphere	Input	FreeSurfer	Spherical Demons	Non-optimal Ours	Ours
Left	0.0396 ± 0.0014	0.0207 ± 0.0017	0.0213 ± 0.0022	0.0185 ± 0.0020	0.0182 ± 0.0019
Right	0.0388 ± 0.0015	0.0201 ± 0.0015	0.0207 ± 0.0021	0.0182 ± 0.0016	0.0181 ± 0.0014

with and without an optimal rigid alignment; i.e., the coefficients at $l = 0$ were updated only at the initial guess and excluded during the full optimization.

Fig. 5 shows the average *hCurv* features, and the average variance of *hCurv* is summarized in Table 2. In the three methods, the overall cortical folding patterns of the average map are similar to those of the template, while the proposed method provides the sharpest patterns on the average map as shown in Fig. 5. On the other hand, we could not find noticeable difference in the proposed method between with and without the optimal rigid alignment. Fig. 6 illustrates an example of registration by these methods. They begin with almost the same optimal rigid alignment

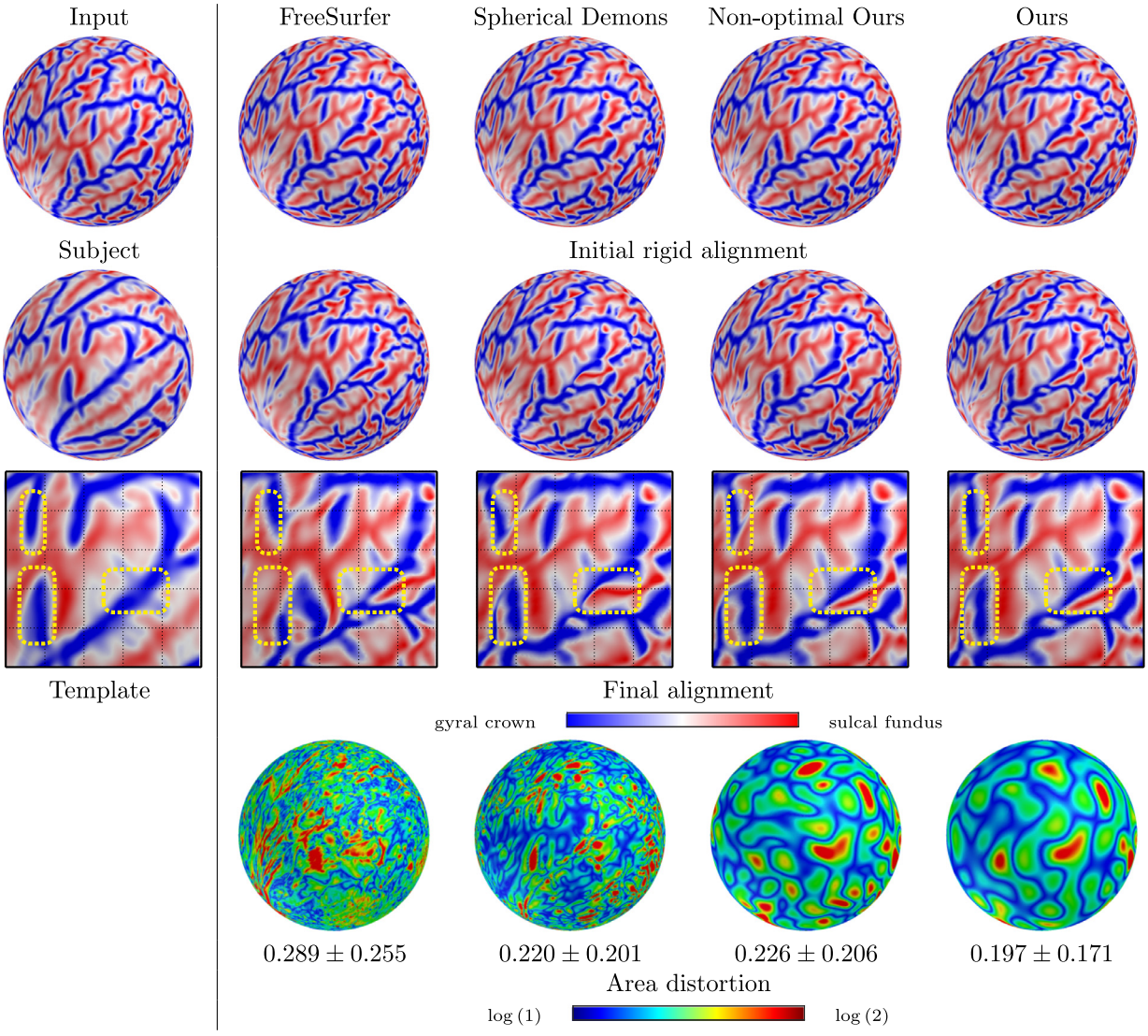

Fig. 6. An example of pair-wise registration from a single subject to a fixed template. These methods begin with almost the same rigid alignment before the local deformation and produce similar *hCurv* patterns with slight difference. However, FreeSurfer and Spherical Demons only update the local deformation during the optimization. This results in relatively large deformation in several regions, whereas the proposed method updates both rigid and non-rigid deformation to reduce locally focused deformation. Also, the optimal rigid alignment in our method provides improved feature alignments and registration distortion compared to ours with a non-optimal rigid alignment.

Table 3
Registration distortion: absolute log ratio (mean ± std) in surface area and edge length. The proposed method yields less registration distortion than FreeSurfer and Spherical Demons with statistical significance ($^*p < .05$).

Metric	Hemisphere	FreeSurfer	Spherical Demons	Non-optimal Ours	Ours
Area	Left	0.278 ± 0.024	0.227 ± 0.010	0.199 ± 0.033	$0.183 \pm 0.018^*$
	Right	0.266 ± 0.028	0.225 ± 0.010	0.181 ± 0.023	$0.175 \pm 0.017^*$
Length	Left	0.165 ± 0.012	0.134 ± 0.005	0.126 ± 0.017	$0.118 \pm 0.011^*$
	Right	0.158 ± 0.015	0.132 ± 0.005	0.117 ± 0.013	$0.114 \pm 0.010^*$

before the local deformation, but the proposed method yields a better local feature alignment after optimizing both rigid and non-rigid deformation.

Finally, we measured area and length distortion for each triangle and edge as the absolute log ratio between before and after registration (Van Essen, 2005; Robinson et al., 2018). We measured such distortion metrics before and after registration for each individual subject. The distortion of each method is summarized in Table 3. The proposed method achieves the smallest distortion for both area and length after two-sided paired *t*-tests (30 samples). The optimization at $l = 0$ slightly improves the overall distortion as well (see Fig. 6 for example) despite statistical significance. Note that the feature alignment and registration distortion in the pair-wise approach are not necessarily small enough since we used a fixed template, to which deformation fields always have a bias. Therefore, the deformation reported in this approach should be interpreted for relative comparisons across the three methods.

3.3. Group-wise registration

We evaluated the three methods in a group-wise manner that reduces a bias toward template selection and provides a sharp

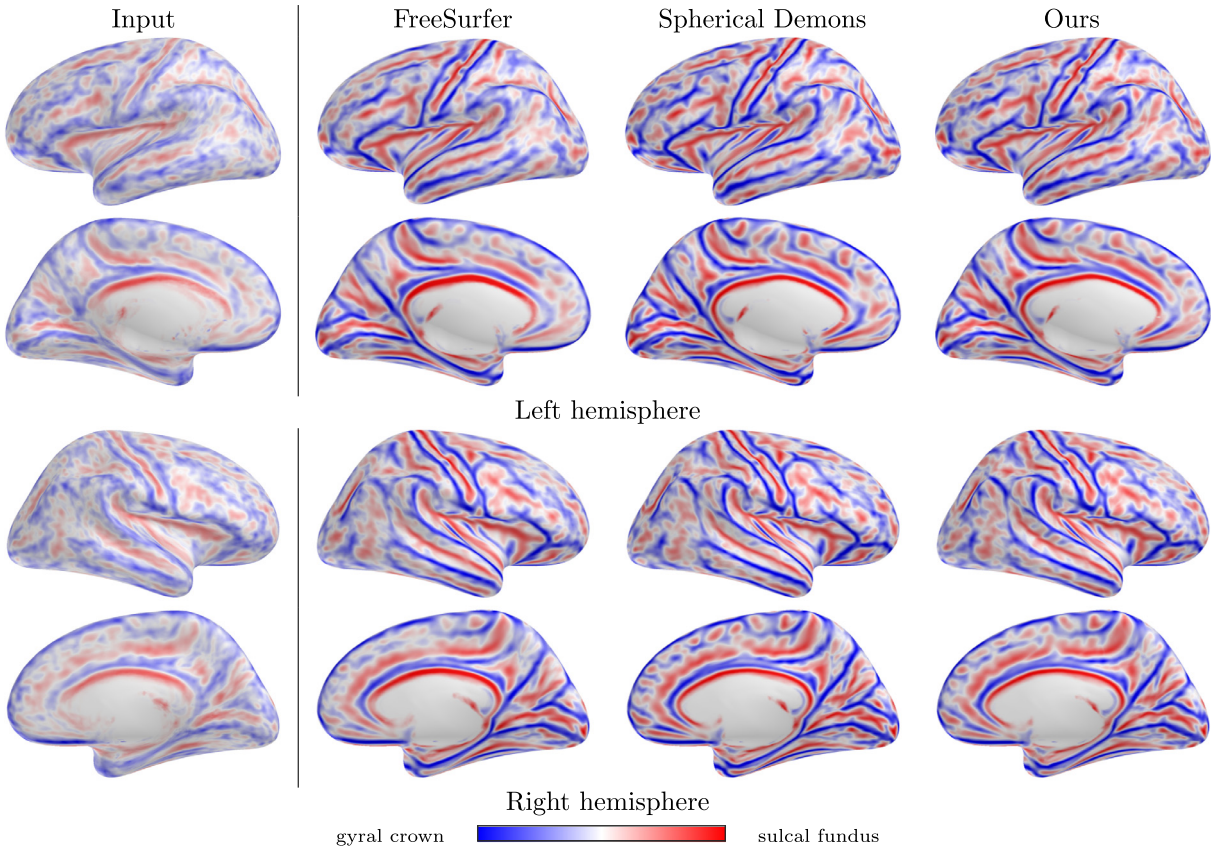

Fig. 7. The average *hCurv* feature maps on the 30 subjects. The three methods achieve similar *hCurv* patterns, while FreeSurfer shows little more blurred patterns than other methods. These methods provide much more improved average patterns than the initial average.

feature mean with low registration distortion. This approach is quite similar to pair-wise registration except that a template is updated after each round of co-registration (Lyttelton et al., 2007). Yeo et al. (2010) used this approach in their work for best performance of Spherical Demons, and FreeSurfer also provides the same procedure for iterative update of the template for group-wise registration in their implementation. For optimal registration and best performance of these methods, we focus on a group-wise approach in the remainder of the experiments at this point.

3.3.1. Feature alignment

We computed the registration results using *lSulc, hSulc, lCurv*, and *hCurv* features of the FreeSurfer's outputs that are optimized for FreeSurfer and Spherical Demons. Once again, the registration in these methods was achieved in a multi-resolution manner by aligning *lCurv* and *lSulc* maps followed by *hSulc* and *hCurv* maps, and we used a different resolution for each feature map with icosahedral subdivision from 4 ($S = 2,562$) to 7 ($S = 163,842$). In each resolution, we optimized spherical harmonics coefficients and fed them as an initial guess to the higher resolution. It is noteworthy that exactly the same feature maps were used for all the methods for fair comparisons. In terms of optimization, their methods estimate a reference template (population average) only before registration; thus, it is fixed during the entire optimization, which requires several rounds of co-registration. In our experiments, the optimization of their methods converged after 3 rounds. Unlike these methods, only a single round of co-registration was sufficient in our method. Indeed, we could not find any noticeable difference after a single round since the population average was semi-optimized after an initial guess. This yields much faster registration than the two methods. In particular, at each round including four features, the proposed method and Spherical Demons took about 15 mins per subject, whereas FreeSurfer took more than an hour per subject after the multi-resolution optimization with the four features. Although Spherical Demons and the proposed method achieved comparable computation time for individual subject registration, FreeSurfer, Spherical Demons, and the proposed method took about 90 hours, 21 hours, and 7 hours for the entire subjects, respectively, after all rounds of co-registration. Fig. 7 shows the average *hCurv* features. It can be observed that overall patterns are quite similar while slightly different patterns (e.g., cingulate sulcus) are exhibited in the three methods. Table 4 summarizes statistics on *hCurv* variance in the three methods. FreeSurfer achieves relatively high variance, which results in little more blurred average patterns than other methods. We found that the proposed method achieves smaller variance for $l \geq 19$ than Spherical Demons (see Fig. 8) for both hemispheres.

3.3.2. Cortical surface parcellation

We evaluated registration performance using cortical parcellation that is completely independent of registration metric. Since no ground-truth parcellation was available, we computed the mode (majority vote) parcellation map across the subjects after performing each surface registration method. Ideally, the parcellation map is completely aligned with all subjects if a surface correspondence is perfectly established. To measure the performance, we computed a Dice coefficient for each region with the mode map. We then performed one-sided paired *t*-tests for the 30 subjects with FreeSurfer and Spherical Demons to reveal regions with statistically significant improvement on Dice coefficients. In this evaluation, we measured Dice coefficients over the entire cortex (30 samples (average Dice coefficient of 49 regions per subject) - a

Table 4
hCurv variance. FreeSurfer shows relatively high variance while Spherical Demons achieves the smallest variance. Here we computed the variance at $l = 15$ for both hemispheres. See Fig. 8 for *hCurv* variance at different degree *l*.

Hemisphere	Input	FreeSurfer	Spherical Demons	Ours
Left	0.0199 ± 0.0088	0.0142 ± 0.0094	0.0113 ± 0.0097	0.0121 ± 0.0100
Right	0.0194 ± 0.0086	0.0138 ± 0.0092	0.0109 ± 0.0093	0.0117 ± 0.0095

Table 5
Overall Dice coefficient in cortical surface parcellation (mean ± std, unit: %). For the right hemisphere, marginal difference is observed from FreeSurfer ($p = .102$), but the proposed method achieves better overlaps on the left hemisphere ($^*p < .05$). Also, the proposed method shows better overlaps on both hemispheres than Spherical Demons ($^\dagger p < .05$).

Hemisphere	FreeSurfer	Spherical Demons	Ours
Left	79.93 ± 2.25	80.27 ± 2.26	$80.61 \pm 2.13^{*\dagger}$
Right	80.15 ± 1.95	80.14 ± 2.01	$80.31 \pm 1.94^{\dagger}$

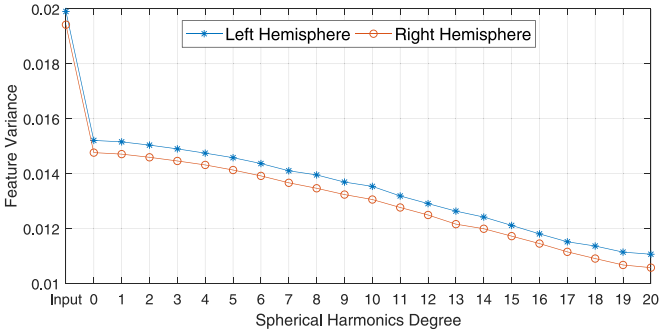

Fig. 8. *hCurv* variance at different degree *l*. The feature variance decreases as *l* increases. Both hemispheres have similar variance at each degree. The proposed method has smaller variance then FreeSurfer and Spherical Demons at $l \geq 9$ and $l \geq 19$, respectively. It is noteworthy that smaller variance does not necessarily indicate better surface registration performance. In our experiments, the proposed method works well at $l = 15$ in terms of cortical parcellation and registration distortion.

single test for each method) and for each cortical region (30 samples for each region - 49 tests for each method). For the latter evaluation, we further corrected *p*-values with respect to the number of regions via a standard false discovery rate (FDR) (Benjamini and Hochberg, 1995) at $q = .05$. Since the one-sided test tells which method has significant improvement, we setup two different hypotheses on Dice coefficients: the proposed method is better than the existing method and the proposed method is worse than the existing method. Table 5 summarizes the average Dice coefficients on the entire cortex across the 30 subjects. Althoguh the improvement was not considerable, the statistical tests revealed that our method achieves significant improvement on the left hemisphere and both hemispheres over FreeSurfer and Spherical Demons, respectively ($p < .05$). For the right hemisphere, marginal difference was observed from FreeSurfer ($p = 0.102$). Several significantly improved regions were revealed, while no region was found with significantly decreased overlaps. Figs. 9 and 10 show the detailed Dice coefficients and their corresponding regions, respectively. Our method shows better overlaps particularly on the motor cortex and temporal lobe on both hemispheres.

3.3.3. Registration distortion

As in the evaluation on the pair-wise registration, we measured area and length distortion for each triangle and edge as the absolute log ratio between before and after registration. We then collected all the measurements to compute their distribution. Table 6 summarizes registration distortion (30 samples - average distortion per subject) in the three methods. Our method provides significantly reduced registration distortion compared to FreeSurfer and Spherical Demons. For both hemispheres, the maximum area change (i.e., exponential of the area distortion) across subjects was smaller than FreeSurfer and Spherical Demons by a factor of about 2.2×10^4 and 2.7, respectively. Similarly, our method also achieves smaller maximum edge change than FreeSurfer and Spherical Demons by a factor of about 3.3×10 and 1.1, respectively. We also measured a moment coefficient of skewness (Pearson, 1895; Kenney and Keeping, 1954) of the distributions in registration distortion as summarized in Table 7. The resulting coefficients indicate that the proposed method has a less skewed distribution to the right (shorter tail), which implies a fewer number of regions with large registration distortion than the other methods. Figs. 11 and 12 show the detailed distributions of the registration distortion. It can be observed from the skewness that the proposed method yields less registration distortion in the resulting deformed spheres for both area and length distortion.

Table 7
Moment coefficient of skewness of the distributions in registration distortion (area and length). The proposed method has a less skewed distribution to the right. This implies that the proposed method has a fewer number of regions with large registration distortion than the other methods. See Figs. 11 and 12 for illustration of the distributions.

Metric	Hemisphere	FreeSurfer	Spherical Demons	Ours
Area	Left	7.572	2.048	1.634
	Right	6.768	2.046	1.646
Length	Left	4.165	1.788	1.682
	Right	3.970	1.857	1.643

In addition, we computed the average of area change in each individual region of the cortical parcellation. This metric measures the amount of absolute area change (combining both compression and expansion) within each region after registration. Since triangle size of FreeSurfer's surfaces is irregular in general, we used the weighted average of area change per each region, where the

Table 6
Registration distortion: absolute log ratio (mean ± std (max)) in surface area and edge length. The proposed method yields less registration distortion than FreeSurfer and Spherical Demons with statistical significance ($^*p < .05$). See Figs. 11 and 12 for detailed statistics.

Metric	Hemisphere	FreeSurfer	Spherical Demons	Ours
Area	Left	0.201 ± 0.011 (12.897)	0.190 ± 0.009 (3.753)	0.182 ± 0.016 (2.503)*
	Right	0.197 ± 0.012 (13.207)	0.190 ± 0.009 (4.095)	0.178 ± 0.017 (2.357)*
Length	Left	0.129 ± 0.006 (6.653)	0.126 ± 0.005 (2.284)	0.124 ± 0.009 (2.088)*
	Right	0.126 ± 0.008 (5.671)	0.126 ± 0.006 (2.105)	0.121 ± 0.009 (2.044)*

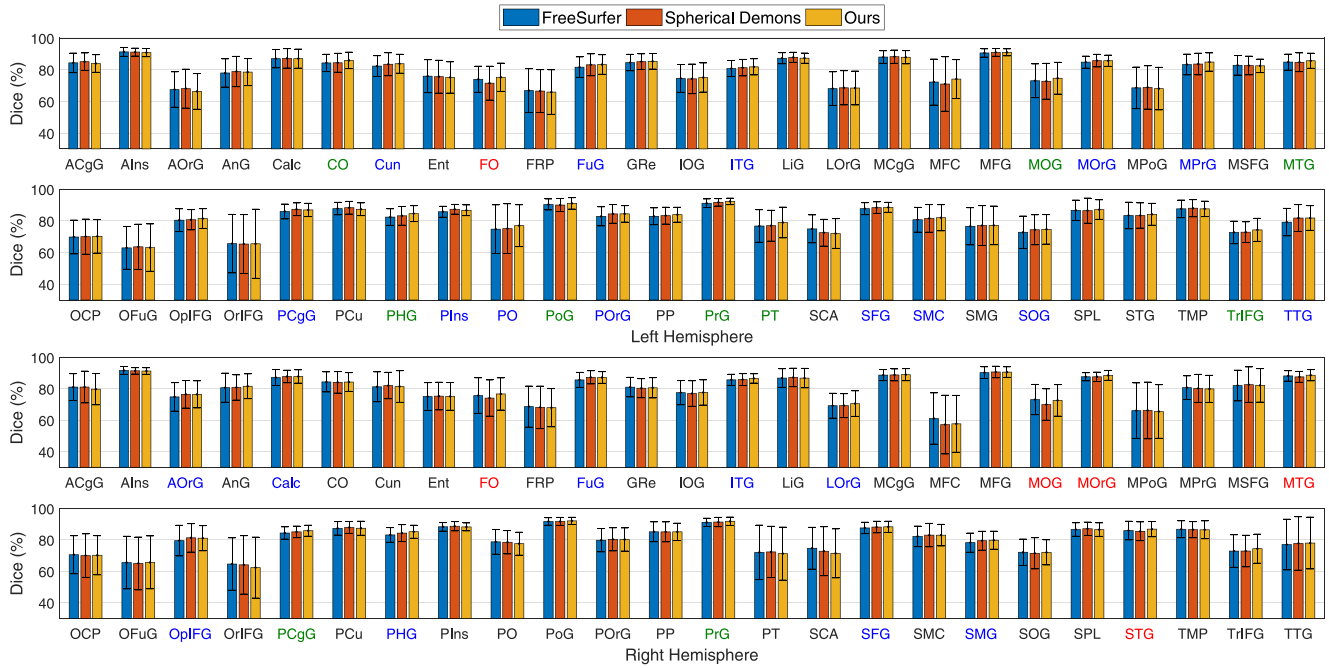

Fig. 9. Dice coefficient of 49 regions on the left and right hemispheres (unit: %). One-sided *t*-tests reveal regions with statistical significance after the FDR correction ($q = .05$). Several regions are significantly improved, while no region becomes worse after the FDR correction. The color in the labels indicates the improved regions compared to FreeSurfer (*blue*), Spherical Demons (*red*), and both methods (*green*). In comparison with FreeSurfer, our method has 21 and 12 improved regions for the left and right hemispheres, and with Spherical Demons, our method has 9 and 7 improved regions for the left and right hemispheres (see Fig. 10 for the improved regions with the adjusted *p*-values). (For interpretation of the references to color in this figure legend, the reader is referred to the web version of this article.)

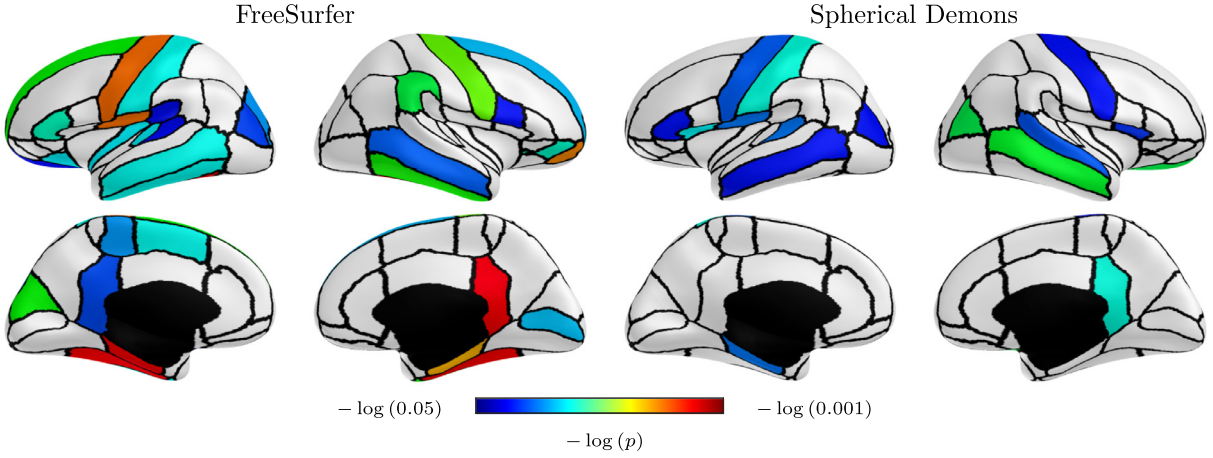

Fig. 10. Negative log of the adjusted *p*-values on cortical regions with significantly improved Dice coefficients after the FDR correction ($q = .05$). The average surface is divided by the mode map of 49 regions. Total 33 and 16 out of 98 regions are significantly improved compared to FreeSurfer and Spherical Demons, respectively. The color indicates negative log of the adjusted *p*-values in the improved regions.

weight is proportional to triangle size. We then performed one-sided paired *t*-tests for the 30 subjects with FreeSurfer and Spherical Demons to reveal regions with significantly reduced distortion. For each method, we performed a single test on average distortion (30 samples) and 49 tests for all cortical regions (30 samples per region). Fig. 13 summarizes the statistics across the 30 subjects, and Fig. 14 shows the corresponding improved regions after the FDR correction ($q = .05$). For each hemisphere, we found that more than a one third of 49 regions have significantly less area change than the other methods, while no region has more area change after the FDR correction. For example, FreeSurfer shows quite huge deformation in Ent (51.52%), whereas relatively much low deformation (15.43%) is measured in the proposed method for both hemispheres. It is noteworthy that the proposed method offers the Dice coefficients on Ent even with significantly low deformation (see Figs. 9 and 15). For another instance in PrG, the proposed method shows less area change (19.99%) with higher Dice coefficients than Spherical Demons (25.20%) for both hemispheres. We emphasize that such reduced area change is achieved while keeping comparable registration accuracy to the other methods.

4. Discussion

4.1. Deformation field

The smoothness of the proposed deformation field is controlled directly by spherical harmonics degree *l*. In our framework, the smoothness does not refer to an additional energy term. Rather, it could be considered conceptually akin to iterative smoothing of the deformation fields proposed in Spherical Demons (Yeo et al., 2010). Yet, the proposed method works in a top-down manner (i.e., from global to local deformation) opposite to Spherical Demons

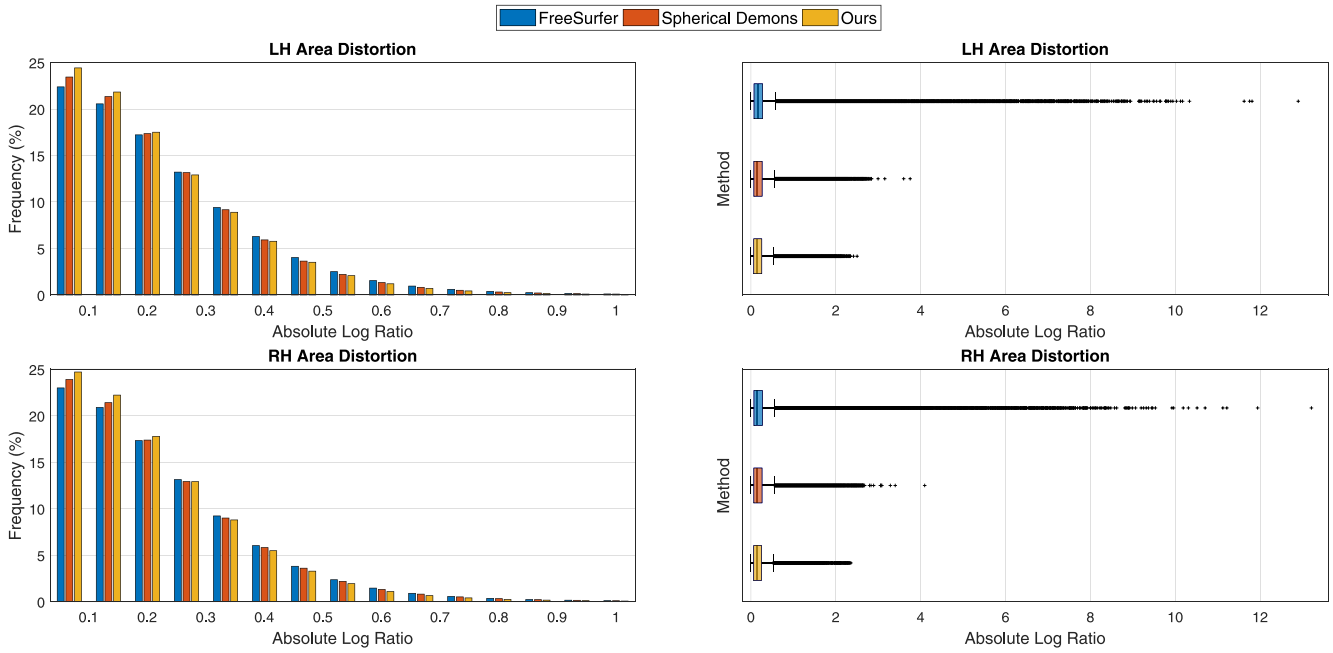

Fig. 11. Area distortion (whiskers with maximum 1.5 interquartile range). The proposed method has a less skewed distribution to the right (shorter tail). This implies a fewer number of regions with large area distortion than FreeSurfer and Spherical Demons on both hemispheres.

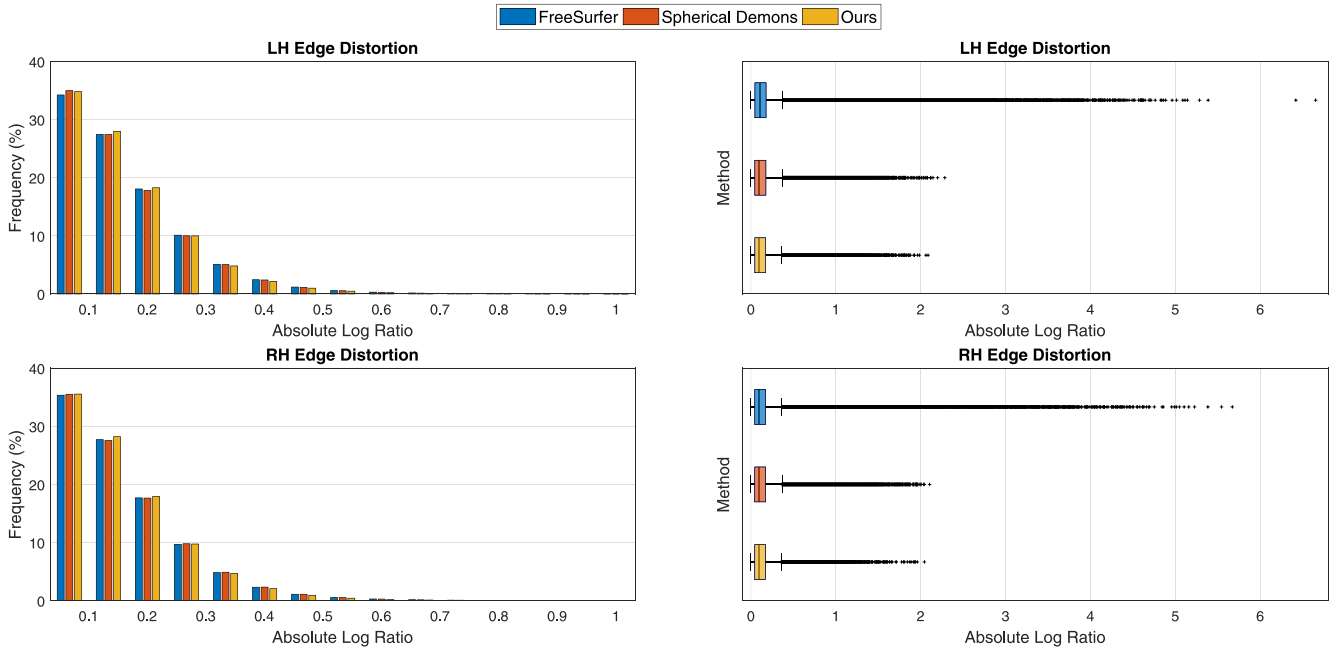

Fig. 12. Edge distortion (whiskers with maximum 1.5 interquartile range). The proposed method has a less skewed distribution to the right (shorter tail). This implies a fewer number of regions with large edge distortion than FreeSurfer and Spherical Demons on both hemispheres.

that performs iterative smoothing on deformation fields after local deformation. Theoretically, the deformation has no interaction with local neighbors if l goes to infinity in our method and if no iteration is given in Spherical Demons.

We found that the energy function decreases as l increases. The proposed method achieved less variance of feature maps for $l \geq 19$. Yet, it still remains unclear about the amount of the smoothness for an optimal shape correspondence since true trajectory of cortical surface deformation is unknown; indeed, this issue has arisen in most surface registration frameworks. For example, our experiments showed comparable overall Dice coefficients of the three methods (Table 5) even though the cortical folding patterns on the average feature maps were slightly different (Fig. 7). As discussed in Yeo et al. (2008), small variance does not always indicate best performance of surface registration. It is also true in the proposed method since better performance was shown at $l = 15$ in terms of cortical parcellation and registration distortion. In several clinical studies (e.g., functional MRIs), there could be different optimal smoothness and thus structural parcellation might not be a good metric for the evaluation on surface registration as discussed in Robinson et al. (2018). Although the proposed method was evaluated on structural parcellation, the orthonormality of spherical

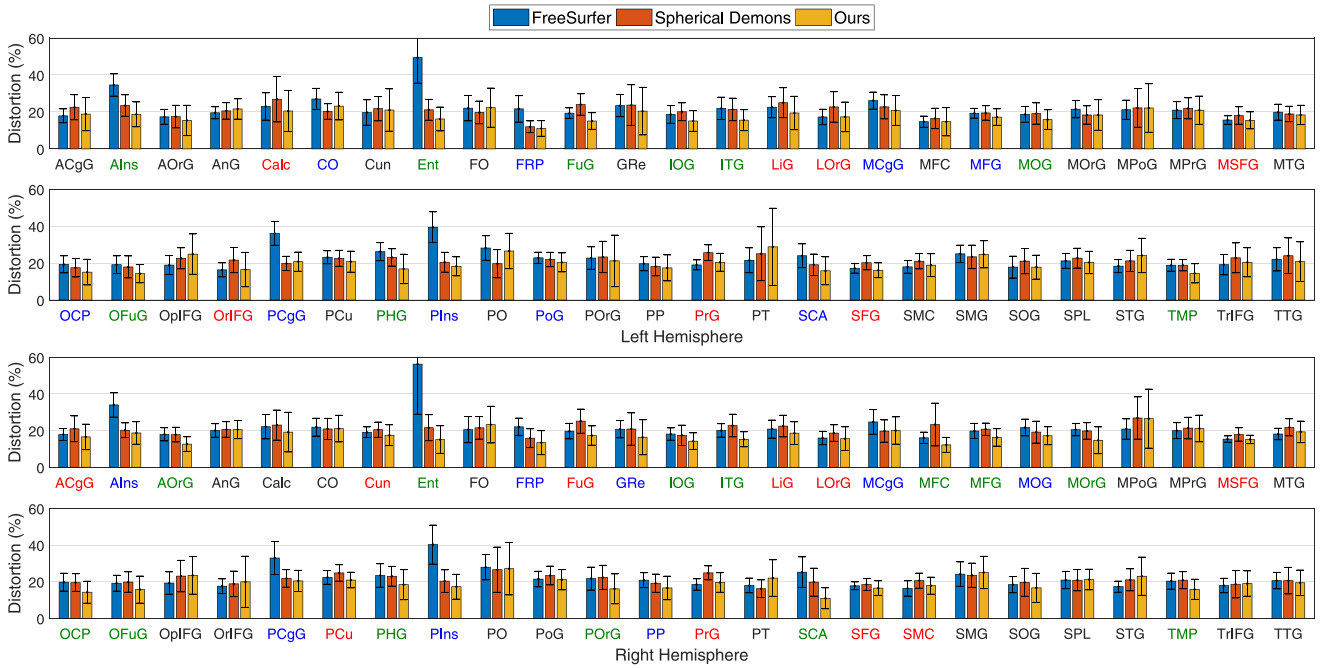

Fig. 13. Area change of 49 regions on the left and right hemispheres (unit %). One-sided *t*-tests reveal regions with statistical significance after the FDR correction ($q = .05$). More than a one third of regions have significantly reduced area change, while no region becomes worse after the FDR correction. In comparison with FreeSurfer, our method has 18 and 21 improved regions for the left and right hemispheres, and with Spherical Demons, our method has 16 and 23 improved regions for the left and right hemispheres (see Fig. 14 for the improved regions with the adjusted *p*-values). Note that the maximum range is truncated at 60% for better visualization. The color in the labels indicates the improved regions compared to FreeSurfer (*blue*), Spherical Demons (*red*), and both methods (*green*). (For interpretation of the references to color in this figure legend, the reader is referred to the web version of this article.)

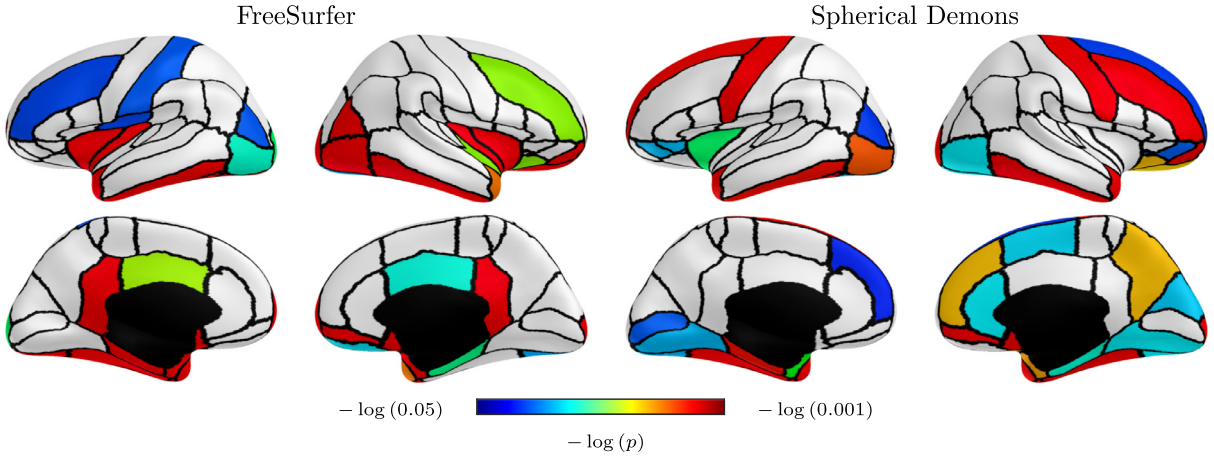

Fig. 14. Negative log of the adjusted *p*-values on cortical regions with significantly reduced area change after the FDR correction ($q = .05$). The average surface is divided by the mode map of 49 regions. Total 39 out of 98 regions are significantly improved compared to FreeSurfer and Spherical Demons. The color indicates negative log of the adjusted *p*-values in the improved regions.

harmonics basis functions can easily control the smoothness of deformation in an easier way than other existing methods, which might be useful to investigate optimal smoothness for other studies.

4.2. Cortical surface parcellation

We used 30 subjects with their ground-truth volumetric labels that were manually corrected after their projection onto the surfaces. In the experiments, we found marginal difference in the average Dice coefficients (up to 0.7% improvement) despite statistical significance. Similarly, our method showed comparable average Dice coefficients to those of the other two methods on Mindboggle-101 (up to 0.3% improvement) despite statistical significance (see supplementary information for the detailed Dice coefficients and their statistics). Statistically, no region was revealed with decreased Dice coefficients on the dataset with BrainCOLOR whereas those in several regions became decreased on Mindboggle-101 despite still inconsiderable absolute difference. Although their direct comparison is non-trivial due to the disparity in the data acquisition (demographics, scan devices, parcellation protocols, etc.), the decreased Dice coefficients were found on Mindboggle-101 mainly because both the increased number of samples (from 30 to 101) and the decreased number of cortical regions (from 49 to 31) increase statistical power, which results in statistical significance even on small absolute difference in the Dice coefficients. Therefore, given such marginal difference in both parcellation protocols, it is difficult to choose the best among the three methods with superior performance. They offer

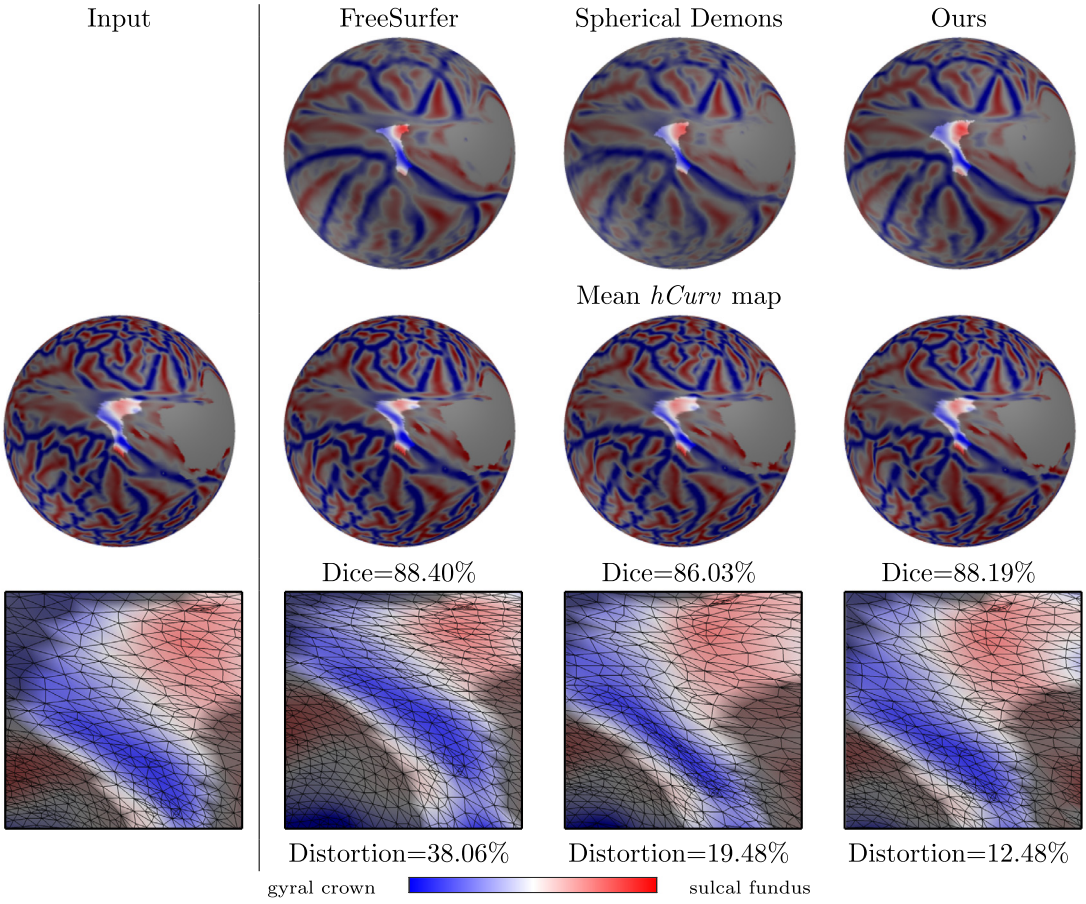

Fig. 15. An example area change in Ent. (*top*) The three methods yield similar cortical folding patterns after co-registration (see Fig. 7 for the average *hCurv* maps). The mode regions of Ent are highlighted brightly. (*middle*) The Dice coefficients are comparable, which implies that these methods achieve comparable performance in surface alignment; the *hCurv* maps are also well aligned with the averages. (*bottom*) Even with comparable registration performance, the surface area (triangle size) is less distorted in the proposed method than FreeSurfer and Spherical Demons. It is noteworthy that the mode region of Ent in our group-wise framework is little larger than others because the distortion can be better minimized (i.e., better area preservation) in this way, while maintaining comparable registration accuracy (see Fig. 9 for Ent).

comparable registration performance in a context of cortical surface parcellation.

4.3. Registration distortion

We evaluated registration distortion for both entire cortical regions and each individual region of the cortical parcellation. The proposed method showed significantly smaller distortion than the other methods, and more than a one third of the cortical regions have significantly lower area change (Figs. 13 and 14) while achieving comparable Dice coefficients (Figs. 9 and 10). This advantage could be desirable in some ROI-based studies that focus on structural or functional analyses within less distorted regions, in which cortical surface quantification (e.g., cortical thickness) can be also resampled with less distortion. The further importance about distortion has been discussed in Van Essen (2005). In our experiments, however, we excluded vertex-wise registration distortion at each corresponding location since inter-subject variability in distortion was quite arbitrary in the three methods (see Fig. 6 for example). From our observations, the corresponding locations not necessarily have similar amount of the registration distortion along cortical folding. To the best of our knowledge, it is unknown yet that registration distortion is captured in a sense of population average or necessarily similar across the corresponding locations. Deeper investigation into registration distortion would be informative for further shape analyses.

4.4. Optimization

In general, the energy function is non-convex. In our framework, a large number of spherical harmonics coefficients $3(l+1)^2 \cdot N$ need to be optimized, in which a chance to be trapped in local optima is proportional to $3(l+1)^2 \cdot N$. To reduce this chance, we optimized individual degree independently to begin with a reasonable initial guess. This is feasible due to the orthonormality of spherical harmonics basis functions. Thus, the reduced degree of freedom in the optimization can yield better estimation of the coefficients than optimizing over the entire coefficients from the beginning without an initial guess.

In addition to the incremental optimization, we employed a Levenberg-Marquardt optimizer that approximates the second order of the energy function for two reasons. First, the optimizer offers fast convergence in few steps as it behaves like a gradient decent and then turn into a Gauss-Newton optimizer for better convergence. Second, since the Jacobian $\mathbf{J}_f$ and $\mathbf{J}_d$ consist of different signs, the Hessian approximation $\mathbf{H}$ is positive semi-definite, which potentially lacks a full rank. These are handled by a single damping factor λ. Unfortunately, finding an optimal damping factor is non-trivial in most optimization problems including ours, and derivation of its analytic solution is practically implausible. We empirically adjust this variable at each optimization step. λ decreases by a half if the energy is reduced; otherwise, it increases by a factor of 2. Such a simple approach practically worked quite well. Mostly, the optimization is done in 20 steps at each degree

(including full degree optimization). Although we did not extensively investigate parameter tuning in this work, it could be an interesting topic for future work.

4.5. Pair-wise spherical deformation

The three methods offer a well-fitted rigid alignment before the spherical deformation; we could not find significant difference across them after their rigid alignment. Unlike FreeSurfer and Spherical Demons that update only local deformation, the proposed method optimizes both rigid and non-rigid deformation. This might yield relatively locally focused deformation in the other methods, whereas the proposed method shows overall smooth deformation across the cortex (see distortion in Fig. 6). In the experiments, we observed the impact of the optimal rigid alignment by excluding $l = 0$ during the full optimization. Technically, the exclusion of only $l = 0$ is separation between rigid and non-rigid deformation, but spherical harmonics bases at low degrees act close to global (i.e., nearly rigid alignment). Therefore, we found slight difference between with and without a fully optimized rigid alignment on the registered cortical patterns, while the optimal rigid alignment still reduces the amount of the distortion after the registration.

4.6. Group-wise registration

A group-wise approach is independent of a template choice unlike a pair-wise approach. In the optimization, co-registration is performed with the mean and variance of features are estimated from the study group of interest. In this way, the inter-subject variability could be better handled. Therefore, the resulting registration reduces a bias toward a specific template as well as registration distortion. Particularly, the energy function encodes both feature matching and rigidity of deformation, in which the feature mean $\bar{f}$ and variance σ_f^2 are updated during the optimization. In our earlier work (Lyu et al., 2015), they were updated at every iteration step to estimate a population average. However, there is no regularization (or boundary condition) of the estimated average feature map unlike template-based surface registration methods that use a fixed average feature map. In this unconstrained optimization the energy function can be minimized by expanding less variable regions (e.g., regions along the inter-hemispheric cut). Such deformed regions consequently can yield large registration distortion, which might be an undesirable property. In the proposed method, these quantities were instead estimated in two phases at the initialization and after the individual degree optimization. Although our current approach uses a fixed average feature map to prevent large deformation during the optimization of each individual degree, the two-phase average update steps were sufficient in the experiments; a single round of co-registration sufficiently achieved a comparable shape correspondence to the existing methods. Thus, this yields faster convergence to the population average than other methods. In this work, the proposed deformation has a high degree of freedom since spherical harmonics coefficients are unconstrained. We thus introduced an additional regularization term for rigidity of deformation. This term enables more explicit rigidity by maintaining initial relative distances. A main challenge in this regularization is to define distortion prior σ_d^2. Unlike other parameters, σ_d^2 is quite subject-dominant, so its estimation is difficult from a given population. The spherical deformation becomes a rigid rotation as σ_d^2 decreases. In our framework, we empirically set $\sigma_d = 0.04$ corresponding to roughly 4 times the average edge length (0.01) of the triangular mesh of the unit sphere.

4.7. Diffeomorphism

Diffeomorphic surface registration has a differentiable one-to-one mapping between surfaces, which holds several nice properties particularly including no fold (i.e., positive determinant of Jacobian) in a deformation field. In the proposed method, it can be easily shown that the deformation field is differentiable since spherical harmonics basis functions essentially have C^∞ smoothness thanks to trigonometric functions. Unfortunately, the proposed deformation cannot always hold a one-to-one mapping since there is no specific regularization of the Jacobian determinant. This can sometimes happen at a high degree of spherical harmonics if multiple points are mapped onto the same location by the deformation. A possible solution is to maintain the positive Jacobian determinant during the optimization. However, its analytic derivation is quite challenging, so practically implausible. Alternatively, this can be addressed by unfolding a deformation field by finding triangles with negative area after registration (Fischl et al., 1999; Yeo et al., 2010; Robinson et al., 2018). In this work, however, unfolding a deformation field cannot be directly incorporated in a sense of spherical harmonics interpolation since the approach locally modifies a deformation field. We instead reduced the update step size δ in a Levenberg-Marquardt framework, which limits the amount of deformation. Yet, all of these approaches are still empirical and theoretically might not completely obey diffeomorphism. In practice, these can hold diffeomorphism in the discrete domain (Yeo et al., 2010). Once a one-to-one mapping is guaranteed, there exists an inverse mapping in the proposed deformation, which is just a transpose of local rotation matrices.

4.8. Implementation issues

The computation time of the proposed method depends mainly on deformation field update and Hessian approximation. To update deformation fields at each iteration, local rotations need to be recomputed, which guides deformation of the spheres. Since deformation fields change over time, we need to know the corresponding locations to the icosahedral sampling points for each individual sphere. This requires an efficient triangle search algorithm on the unit sphere. Naive exhaustive search is infeasible in practice due to a large number of triangles (320k). To expedite triangle search, we used a customized axis-aligned bounding box (AABB) hierarchy, in which spherical locations are represented by spherical polar coordinates. In this way, the search dimension is reduced from 3D to 2D, and the search becomes faster and more efficient because the bounding boxes tightly cover only spherical regions. In our implementation, the AABB hierarchy update takes less than a second.

The Hessian approximation needs Jacobian of the energy function, and its computation requires $O(S^2 \cdot (l+1)^2)$ time complexity. At the end of optimization, the number of sampling points S is approximately 160k and that of spherical harmonics coefficients is 256×3 at $l = 15$. In our implementation, the Basic Linear Algebra Subprograms (BLAS) routines provided great efficiency on computing this step (about 5 seconds per subject at full degree optimization on a single core). In addition to the time complexity, this step requires $O(S \cdot (l+1)^2)$ space, which indicates that l has a quadratic space complexity. It consumes about 500 Mbytes memory per subject in our implementation. For a large population, therefore, l needs to be determined according to memory capacity to avoid potential overflow if memory capacity is limited.

Finally, all computation steps are independent. Thus, these already have a good shape of parallelism. We implemented GPU matrix computation for the Hessian approximation, which reduces the processing time by a half. Note that the implementation was not used for the comparisons in our experiments. GPU acceleration can be also applied to the AABB hierarchy update/query since every

triangle is treated independently as a single node (Popov et al., 2007). We expect that a GPU version of the AABB hierarchy will provide better efficiency.

5. Conclusion

We presented novel hierarchical spherical deformation for cortical surface registration. Motivated by the composition of precession and intrinsic rotation, the proposed method extends the composite rigid rotation to general non-rigid deformation as functions of spherical locations. To this end, we used spherical harmonics interpolation of local rigid rotations to generate smooth non-rigid deformation fields. By optimizing spherical harmonics coefficients, optimal rigid and non-rigid deformation is achieved simultaneously in a single framework. To allow rigid rotations more explicitly, we further introduced an additional regularization term of the rigidity. Also, we derived the second order approximation of the energy function for better convergence of the optimization. Consequently, the resulting deformation is smooth, continuous, and independent of a particular spherical coordinate system. The proposed method is template-free group-wise registration that avoids a potential bias toward template selection. In the experiments, the proposed method showed a comparable feature map alignment to other state-of-the-art methods. In addition, the proposed method achieved high accuracy in cortical surface parcellation as well as low registration distortion in terms of surface area and edge length. This low distortion was achieved while providing comparable registration accuracy. Finally, the proposed method offered fast group-wise surface registration, and implementation with a GPU version of the Hessian computation is publicly available.

Declaration of Competing Interest

The authors declare no conflict of interest.

Acknowledgments

This work was supported in part by the National Institutes of Health (NIH) under Grants R01EB017230, R01MH102266, and U54HD079124, in part by VISE/VICTR under Grant VR3029, and in part by NVIDIA Corporation under GPU Grant Program.

Appendix A. Gradients of Spherical Locations

We take derivatives at $\hat{\mathbf{p}} = \varphi(\theta_{\hat{\mathbf{p}}}, \phi_{\hat{\mathbf{p}}})$ with respect to spherical harmonics coefficients. We first consider $c^m_{l,\omega}$. From Eq. (10), we have the following composite partial derivative by the chain rule:

$$\frac{\partial \hat{\mathbf{p}}}{\partial c^m_{l,\omega}} = \frac{\partial \omega}{\partial c^m_{l,\omega}} \cdot \frac{\partial \hat{\mathbf{p}}}{\partial \omega}. \tag{A.1}$$

Since ω is a real-valued function, we have

$$\begin{aligned}\frac{\partial \hat{\mathbf{p}}}{\partial \omega} &= [\hat{\mathbf{z}}]_\times \cdot \exp(\omega[\hat{\mathbf{z}}]_\times) \cdot \exp([\mathbf{z} \times \mathbf{z}_T]_\times) \cdot \mathbf{p} \\ &= [\hat{\mathbf{z}}]_\times \cdot \hat{\mathbf{p}},\end{aligned} \tag{A.2}$$

and Eq. (16) yields

$$\frac{\partial \omega}{\partial c^m_{l,\omega}} = Y_{l,m}(\theta_{\hat{\mathbf{p}}}, \phi_{\hat{\mathbf{p}}}). \tag{A.3}$$

Hence, we have the following form.

$$\frac{\partial \hat{\mathbf{p}}}{\partial c^m_{l,\omega}} = Y_{l,m}(\theta_{\hat{\mathbf{p}}}, \phi_{\hat{\mathbf{p}}}) \cdot ([\hat{\mathbf{z}}]_\times \cdot \hat{\mathbf{p}}). \tag{A.4}$$

Now we consider derivatives with respect to $c^m_{l,\mathbf{u}_1}$. By the chain rule, Eq. (10) becomes

$$\frac{\partial \hat{\mathbf{p}}}{\partial c^m_{l,\mathbf{u}_1}} = \frac{\partial c_{\mathbf{u}_1}}{\partial c^m_{l,\mathbf{u}_1}} \cdot \frac{\partial \hat{\mathbf{p}}}{\partial c_{\mathbf{u}_1}}. \tag{A.5}$$

In general, SO(3) does not hold the commutativity. For easier derivation, we slightly modify Eq. (9) as follows.

$$\mathbf{R}(c_{\mathbf{u}_1}, c_{\mathbf{u}_2}, \omega) = \exp([\mathbf{z} \times \mathbf{z}_T]_\times) \cdot \exp(\omega[\mathbf{z}]_\times). \tag{A.6}$$

This switches the order of rotations but yields a composite rotation equivalent to Eq. (9). From Eq. (4), we expand Eq. (7) by the distributive property.

$$\begin{aligned}\exp([\mathbf{z} \times \mathbf{z}_T]_\times) &= \exp([(c_{\mathbf{u}_1}\mathbf{u}_1 + c_{\mathbf{u}_2}\mathbf{u}_2) \times \mathbf{z}_T]_\times) \\ &= \exp([c_{\mathbf{u}_1}\mathbf{u}_1 \times \mathbf{z}_T + c_{\mathbf{u}_2}\mathbf{u}_2 \times \mathbf{z}_T]_\times).\end{aligned} \tag{A.7}$$

Since $c_{\mathbf{u}_1}$ is a real-valued function, we have

$$\begin{aligned}\frac{\partial \hat{\mathbf{p}}}{\partial c_{\mathbf{u}_1}} &= [\mathbf{u}_1 \times \mathbf{z}_T]_\times \cdot \exp([\mathbf{z} \times \mathbf{z}_T]_\times) \cdot \exp(\omega[\mathbf{z}]_\times) \cdot \mathbf{p} \\ &= [\mathbf{u}_1 \times \mathbf{z}_T]_\times \cdot \hat{\mathbf{p}},\end{aligned} \tag{A.8}$$

and Eq. (15) yields

$$\frac{\partial c_{\mathbf{u}_1}}{\partial c^m_{l,\mathbf{u}_1}} = Y_{l,m}(\theta_{\hat{\mathbf{p}}}, \phi_{\hat{\mathbf{p}}}). \tag{A.9}$$

Hence, we have the following form.

$$\frac{\partial \hat{\mathbf{p}}}{\partial c^m_{l,\mathbf{u}_1}} = Y_{l,m}(\theta_{\hat{\mathbf{p}}}, \phi_{\hat{\mathbf{p}}}) \cdot ([\mathbf{u}_1 \times \mathbf{z}_T]_\times \cdot \hat{\mathbf{p}}). \tag{A.10}$$

We leave out the derivation with respect to $c^m_{l,\mathbf{u}_2}$, which can be derived analogously as that of $c^m_{l,\mathbf{u}_1}$.

Supplementary material

Supplementary material associated with this article can be found, in the online version, at 10.1016/j.media.2019.06.013

References

Agrawal, P., Whitaker, R.T., Elhabian, S.Y., 2017. Learning Deep Features for Automated Placement of Correspondence Points on Ensembles of Complex Shapes. In: International Conference on Medical Image Computing and Computer-Assisted Intervention. Springer, pp. 185–193.

Armstrong, E., Schleicher, A., Omran, H., Curtis, M., Zilles, K., 1995. The ontogeny of human gyrification. Cerebral Cortex 5 (1), 56–63.

Auzias, G., Lefèvre, J., Le Troter, A., Fischer, C., Perrot, M., Régis, J., Coulon, O., 2013. Model-driven harmonic parameterization of the cortical surface: Hip-hop. IEEE Trans. Med. Imag. 32 (5), 873–887.

Benjamini, Y., Hochberg, Y., 1995. Controlling the false discovery rate: a practical and powerful approach to multiple testing. J. R Stat. Soc. Ser. B (Methodol.) 289–300.

Cates, J., Fletcher, P., Styner, M., Shenton, M., Whitaker, R., 2007. Shape Modeling and Analysis with Entropy-Based Particle Systems. In: Karssemeijer, N., Lelieveldt, B. (Eds.), Information Processing in Medical Imaging 2007. Springer, Heidelberg, pp. 333–345.

Choi, P.T., Lam, K.C., Lui, L.M., 2015. Flash: fast landmark aligned spherical harmonic parameterization for genus-0 closed brain surfaces. SIAM J. Imag. Sci. 8 (1), 67–94.

Cointepas, Y., Mangin, J.-F., Garnero, L., Poline, J.-B., Benali, H., 2001. Brainvisa: software platform for visualization and analysis of multi-modality brain data. Neuroimage 13 (6), 98.

Dale, A.M., Fischl, B., Sereno, M.I., 1999. Cortical surface-based analysis: I. segmentation and surface reconstruction. Neuroimage 9 (2), 179–194.

Datar, M., Lyu, I., Kim, S., Cates, J., Styner, M.A., Whitaker, R., 2013. Geodesic Distances to Landmarks for Dense Correspondence on Ensembles of Complex Shapes. In: International Conference on Medical Image Computing and Computer-Assisted Intervention. Springer, pp. 19–26.

Fischl, B., Sereno, M., Tootell, R., Dale, A., 1999. High-resolution intersubject averaging and a coordinate system for the cortical surface. Hum. Brain Mapp. 8 (4), 272–284.

Gahm, J.K., Shi, Y., Initiative, A.D.N., et al., 2018. Riemannian metric optimization on surfaces (rmos) for intrinsic brain mapping in the laplace–beltrami embedding space. Med. Image Anal. 46, 189–201.

Gaser, C., Luders, E., Thompson, P.M., Lee, A.D., Dutton, R.A., Geaga, J.A., Hayashi, K.M., Bellugi, U., Galaburda, A.M., Korenberg, J.R., et al., 2006. Increased local gyrification mapped in williams syndrome. Neuroimage 33 (1), 46–54.

Glaunès, J., Vaillant, M., Miller, M.I., 2004. Landmark matching via large deformation diffeomorphisms on the sphere. J. Math. Imag. Vis. 20 (1–2), 179–200.
Gu, X., Wang, Y., Chan, T.F., Thompson, P.M., Yau, S.-T., 2004. Genus zero surface conformal mapping and its application to brain surface mapping. IEEE Trans. Med. Imag. 23 (8), 949–958.
Haker, S., Angenent, S., Tannenbaum, A., Kikinis, R., Sapiro, G., Halle, M., 2000. Conformal surface parameterization for texture mapping. IEEE Trans. Visualiz. Comput. Graph. 6 (2), 181–189.
Harris, J.M., Yates, S., Miller, P., Best, J.J., Johnstone, E.C., Lawrie, S.M., 2004. Gyrification in first-episode schizophrenia: a morphometric study. Biol.l Psych. 55 (2), 141–147.
Huo, Y., Plassard, A.J., Carass, A., Resnick, S.M., Pham, D.L., Prince, J.L., Landman, B.A., 2016. Consistent cortical reconstruction and multi-atlas brain segmentation. NeuroImage 138, 197–210.
Hurdal, M.K., Stephenson, K., Bowers, P., Rottenberg, D.A., et al., 2000. Coordinate systems for conformal cerebellar flat maps. NeuroImage 11 (5), S467.
Joshi, A.A., Shattuck, D.W., Thompson, P.M., Leahy, R.M., 2007. Surface-constrained volumetric brain registration using harmonic mappings. IEEE Trans.Med. Imag. 26 (12), 1657–1669.
Kenney, J.F., Keeping, E.S., 1954. Mathematics of Statistics - Part One, 3 D. Van Nostrand Company Inc..
Kim, J., Singh, V., Lee, J., Lerch, J., Ad-Dab'bagh, Y., MacDonald, D., Lee, J., Kim, S., Evans, A., 2005. Automated 3-D extraction and evaluation of the inner and outer cortical surfaces using a Laplacian map and partial volume effect classification. NeuroImage 27 (1), 210–221.
Kim, S.H., Lyu, I., Fonov, V.S., Vachet, C., Hazlett, H.C., Smith, R.G., Piven, J., Dager, S.R., Mckinstry, R.C., Pruett Jr, J.R., et al., 2016. Development of cortical shape in the human brain from 6 to 24 months of age via a novel measure of shape complexity. NeuroImage 135, 163–176.
Klein, A., Dal Canton, T., Ghosh, S.S., Landman, B., Lee, J., Worth, A., 2010. Open Labels: Online Feedback for a Public Resource of Manually Labeled Brain Images. 16th Annual Meeting for the Organization of Human Brain Mapping.
Klein, A., Tourville, J., 2012. 101 Labeled brain images and a consistent human cortical labeling protocol. Front. Neurosci. 6, 171.
Landman, B., Warfield, S., 2012. MICCAI 2012 Workshop on Multi-Atlas Labeling. CreateSpace Independent Publishing Platform.
Levenberg, K., 1944. A method for the solution of certain non-linear problems in least squares. Q. Appl. Math. 2 (2), 164–168.
Lombaert, H., Sporring, J., Siddiqi, K., 2013. Diffeomorphic Spectral Matching of Cortical Surfaces. In: Information Processing in Medical Imaging. Springer, pp. 376–389.
Luders, E., Narr, K.L., Thompson, P.M., Rex, D.E., Jancke, L., Steinmetz, H., Toga, A.W., 2004. Gender differences in cortical complexity. Nature Neurosci. 7 (8), 799–800.
Lui, J.H., Hansen, D.V., Kriegstein, A.R., 2011. Development and evolution of the human neocortex. Cell 146 (1), 18–36.
Lyttelton, O., Boucher, M., Robbins, S., Evans, A., 2007. An unbiased iterative group registration template for cortical surface analysis. NeuroImage 34 (4), 1535–1544.
Lyu, I., Styner, M.A., Landman, B.A., 2018. Hierarchical Spherical Deformation for Shape Correspondence. In: International Conference on Medical Image Computing and Computer-Assisted Intervention. Springer, pp. 853–861.
Lyu, I., Kim, S., Girault, J., Gilmore, J., Styner, M., 2018. A cortical shape-adaptive approach to local gyrification index.. Med. Image Anal. 48, 244–258.
Lyu, I., Kim, S.H., Seong, J.-K., Yoo, S.W., Evans, A., Shi, Y., Sanchez, M., Niethammer, M., Styner, M.A., 2015. Robust estimation of group-wise cortical correspondence with an application to macaque and human neuroimaging studies. Front. Neurosci. 9, 210.
Lyu, I., Kim, S.H., Woodward, N.D., Styner, M.A., Landman, B.A., 2018. TRACE: A topological graph representation for automatic sulcal curve extraction. IEEE Trans. Med. Imag. 37 (7), 1653–1663.
Lyu, I., Seong, J., Shin, S., Im, K., Roh, J., Kim, M., Kim, G., Kim, J., Evans, A., Na, D., Lee, J., 2010. Spectral-based automatic labeling and refining of human cortical sulcal curves using expert-provided examples. NeuroImage 52 (1), 142–157.
Mangin, J.-F., Lebenberg, J., Lefranc, S., Labra, N., Auzias, G., Labit, M., Guevara, M., Mohlberg, H., Roca, P., Guevara, P., et al., 2016. Spatial normalization of brain images and beyond. Med. Image Anal. 33, 127–133.
Marcus, D.S., Wang, T.H., Parker, J., Csernansky, J.G., Morris, J.C., Buckner, R.L., 2007. Open access series of imaging studies (oasis): cross-sectional mri data in young, middle aged, nondemented, and demented older adults. J. Cognit. Neurosci. 19 (9), 1498–1507.
Marquardt, D.W., 1963. An algorithm for least-squares estimation of nonlinear parameters. J. Soc. Ind. Appl.Math. 11 (2), 431–441.
Oguz, I., Niethammer, M., Cates, J., Whitaker, R., Fletcher, T., Vachet, C., Styner, M., 2009. Cortical Correspondence with Probabilistic Fiber Connectivity. In: Prince, J., Pham, D., Myers, K. (Eds.), Information Processing in Medical Imaging 2009. Springer, Heidelberg, pp. 651–663.
Orasanu, E., Bazin, P.-L., Melbourne, A., Lorenzi, M., Lombaert, H., Robertson, N.J., Kendall, G., Weiskopf, N., Marlow, N., Ourselin, S., 2016. Longitudinal Analysis of the Preterm Cortex using Multi-Modal Spectral Matching. In: International Conference on Medical Image Computing and Computer-Assisted Intervention. Springer, pp. 255–263.
Park, H., Park, J., Seong, J., Na, D., Lee, J., 2012. Cortical surface registration using spherical thin-plate spline with sulcal lines and mean curvature as features. J. Neurosci. Method. 206 (1), 46–53.
Pearson, K., 1895. Contributions to the mathematical theory of evolution. ii. skew variation in homogeneous material. Philos. Trans. R Soci.London 186 (Part I), 343–424.
Popov, S., Günther, J., Seidel, H.-P., Slusallek, P., 2007. Stackless kd-tree traversal for high performance GPUray tracing. Comput. Graph. Forum 26 (3), 415–424.
Quicken, M., Brechbuhler, C., Hug, J., Blattmann, H., Székely, G., 2000. Parameterization of Closed Surfaces for Parametric Surface Description. In: Computer Vision and Pattern Recognition, 2000. Proceedings. IEEE Conference on, 1. IEEE, pp. 354–360.
Robbins, S., Evans, A.C., Collins, D.L., Whitesides, S., 2004. Tuning and comparing spatial normalization methods. Med. Image Anal. 8 (3), 311–323.
Robinson, E.C., Garcia, K., Glasser, M.F., Chen, Z., Coalson, T.S., Makropoulos, A., Bozek, J., Wright, R., Schuh, A., Webster, M., et al., 2018. Multimodal surface matching with higher-order smoothness constraints. NeuroImage 167, 453–465.
Schmitt, J.E., Watts, K., Eliez, S., Bellugi, U., Galaburda, A.M., Reiss, A.L., 2002. Increased gyrification in williams syndrome: evidence using 3d mri methods. Dev. Med. Child Neurol. 44 (5), 292–295.
Shi, R., Zeng, W., Su, Z., Jiang, J., Damasio, H., Lu, Z., Wang, Y., Yau, S.-T., Gu, X., 2017. Hyperbolic harmonic mapping for surface registration. IEEE Trans. Pattern Anal. Mach.intell. 39 (5), 965–980.
Shi, Y., Tu, Z., Reiss, A.L., Dutton, R.A., Lee, A.D., Galaburda, A.M., Dinov, I., Thompson, P.M., Toga, A.W., 2009. Joint sulcal detection on cortical surfaces with graphical models and boosted priors. IEEE Trans. Med. Imag. 28 (3), 361–373.
Tao, X., Prince, J.L., Davatzikos, C., 2002. Using a statistical shape model to extract sulcal curves on the outer cortex of the human brain. IEEE Trans. Med. Imag. 21 (5), 513–524.
Tardif, C.L., Schäfer, A., Waehnert, M., Dinse, J., Turner, R., Bazin, P.-L., 2015. Multi-contrast multi-scale surface registration for improved alignment of cortical areas. Neuroimage 111, 107–122.
Thompson, P.M., Hayashi, K.M., Sowell, E.R., Gogtay, N., Giedd, J.N., Rapoport, J.L., De Zubicaray, G.I., Janke, A.L., Rose, S.E., Semple, J., et al., 2004. Mapping cortical change in alzheimer's disease, brain development, and schizophrenia. Neuroimage 23, S2–S18.
Tosun, D., Rettmann, M.E., Prince, J.L., 2004. Mapping techniques for aligning sulci across multiple brains. Med. Image Anal. 8 (3), 295–309.
Tsui, A., Fenton, D., Vuong, P., Hass, J., Koehl, P., Amenta, N., Coeurjolly, D., DeCarli, C., Carmichael, O., 2013. Globally Optimal Cortical Surface Matching with Exact Landmark Correspondence. In: Information Processing in Medical Imaging. Springer, pp. 487–498.
Van Essen, D.C., 2005. A population-average, landmark-and surface-based (pals) atlas of human cerebral cortex. Neuroimage 28 (3), 635–662.
Wheland, D., Pantazis, D., 2014. Second order blind identification on the cerebral cortex. J. Neurosci. Methods 223, 40–49.
Wright, R., Makropoulos, A., Kyriakopoulou, V., Patkee, P.A., Koch, L.M., Rutherford, M.A., Hajnal, J.V., Rueckert, D., Aljabar, P., 2015. Construction of a fetal spatio-temporal cortical surface atlas from in utero MRI: application of spectral surface matching. NeuroImage 120, 467–480.
Yeo, B., Sabuncu, M., Vercauteren, T., Ayache, N., Fischl, B., Golland, P., 2010. Spherical demons: fast diffeomorphic landmark-free surface registration. IEEE Trans. Med. Imag. 29 (3), 650–668.
Yeo, B.T., Sabuncu, M.R., Desikan, R., Fischl, B., Golland, P., 2008. Effects of registration regularization and atlas sharpness on segmentation accuracy. Med. image Anal. 12 (5), 603–615.
Zou, G., Hua, J., Muzik, O., 2007. Non-Rigid Surface Registration using Spherical Thin-Plate Splines. In: International Conference on Medical Image Computing and Computer-Assisted Intervention. Springer, pp. 367–374.